Du, J., Chen, C., Lesur, V., Lane, R., Wang, H. (2015): Magnetic potential, vector and gradient tensor fields of a tesseroid in a geocentric spherical coordinate system. - *Geophysical Journal International*, *201*, 3, p. 1977-2007.

DOI: http://doi.org/10.1093/gji/ggv123

Geophysical Journal International

Geophys. J. Int. (2015) **201,** 1977–2007 doi: 10.1093/gji/ggv123

GJI Geomagnetism, rock magnetism and palaeomagnetism

Magnetic potential, vector and gradient tensor fields of a tesseroid in a geocentric spherical coordinate system

Jinsong Du,[1,2] Chao Chen,[1] Vincent Lesur,[2] Richard Lane[3] and Huilin Wang[4]

[1] *Hubei Subsurface Multi-scale Imaging Key Laboratory, Institute of Geophysics and Geomatics, China University of Geosciences, Wuhan* 430074*, China. E-mail: jinsongdu.cug@gmail.com*

[2] *Helmholtz Centre Potsdam, GFZ German Research Centre for Geosciences, Telegrafenberg D*-14473*, Germany*

[3] *Geoscience Australia, Hindmarsh Drive, Symonston, ACT* 2609*, Australia*

[4] *Department of Physics, University of Alberta, Edmonton, AB, T6G* 2*E*1*, Canada*

Accepted 2015 March 10. Received 2015 March 8; in original form 2014 October 16

SUMMARY

We examined the mathematical and computational aspects of the magnetic potential, vector and gradient tensor fields of a tesseroid in a geocentric spherical coordinate system (SCS). This work is relevant for 3-D modelling that is performed with lithospheric vertical scales and global, continent or large regional horizontal scales. The curvature of the Earth is significant at these scales and hence, a SCS is more appropriate than the usual Cartesian coordinate system (CCS). The 3-D arrays of spherical prisms (SP; 'tesseroids') can be used to model the response of volumes with variable magnetic properties. Analytical solutions do not exist for these model elements and numerical or mixed numerical and analytical solutions must be employed. We compared various methods for calculating the response in terms of accuracy and computational efficiency. The methods were (1) the spherical coordinate magnetic dipole method (MD), (2) variants of the 3-D Gauss–Legendre quadrature integration method (3-D GLQI) with (i) different numbers of nodes in each of the three directions, and (ii) models where we subdivided each SP into a number of smaller tesseroid volume elements, (3) a procedure that we term revised Gauss–Legendre quadrature integration (3-D RGLQI) where the magnetization direction which is constant in a SCS is assumed to be constant in a CCS and equal to the direction at the geometric centre of each tesseroid, (4) the Taylor's series expansion method (TSE) and (5) the rectangular prism method (RP). In any realistic application, both the accuracy and the computational efficiency factors must be considered to determine the optimum approach to employ. In all instances, accuracy improves with increasing distance from the source. It is higher in the percentage terms for potential than the vector or tensor response. The tensor errors are the largest, but they decrease more quickly with distance from the source. In our comparisons of relative computational efficiency, we found that the magnetic potential takes less time to compute than the vector response, which in turn takes less time to compute than the tensor gradient response. The MD method takes less time to compute than either the TSE or RP methods. The efficiency of the (GLQI and) RGLQI methods depends on the polynomial order, but the response typically takes longer to compute than it does for the other methods. The optimum method is a complex function of the desired accuracy, the size of the volume elements, the element latitude and the distance between the source and the observation. For a model of global extent with typical model element size (e.g. 1 degree horizontally and 10 km radially) and observations at altitudes of 10s to 100s of km, a mixture of methods based on the horizontal separation of the source and observation separation would be the optimum approach. To demonstrate the RGLQI method described within this paper, we applied it to the computation of the response for a global magnetization model for observations at 300 and 30 km altitude.

Key words: Numerical solutions; Numerical approximations and analysis; Magnetic anomalies: modelling and interpretation; Magnetic field; Satellite magnetics.

1 INTRODUCTION

Forward modelling the magnetic potential and its derivatives caused by a magnetized source is a basic issue in geophysics (e.g. Hall 1959). Among all the models with different geometric shapes, such as point and line sources (Henderson & Zietz 1948), laminae (Talwani 1965), polyhedral bodies (Bott 1963; Barnett 1976; Hansen & Wang 1988) and vertical right cylinder (Singh & Sabina 1978), the prism body is very important as it provides a practical method for approximating a more complex source by the principle of superposition, saturating the source volume without 'holes'. Analytical formulas for the total magnetic field and its derivatives of a prism-shaped body were first presented by Bhattacharyya (1964) and later simplified by Rao & Babu (1991). Sharma (1986) gave expressions for the magnetic potential and vector field components of the Cartesian prism. However, the calculation is very time consuming due to several logarithmic and arctan functions. A significant reduction of computation time can be achieved by applying fast Fourier transform techniques (e.g. Bhattacharyya 1966; Parker 1972; Pedersen 1985; Parker *et al.* 1987; Tontini *et al.* 2009). The price to be paid is a decreasing accuracy when the bounding surface is too rough. An alternative approach is provided by approximate solution of prism integrals, such as the adoption of Gauss–Legendre cubature (e.g. Ku 1977).

Using prisms is especially beneficial for local applications, where height information is generally related to planar Cartesian coordinates referenced to a map projection. However, in regional and even global applications, the curvature of the Earth should be taken into consideration. Traditionally in the SCS, the magnetic field can be calculated both in the frequency domain by spherical harmonic approaches (e.g. Arkani-Hamed & Strangway 1985; Nolte & Siebert 1987; Jackson 1990; Gubbins *et al.* 2011) or spherical cap harmonic approaches (e.g. An & Guan 1990) and in the space domain flexibly by the MDs (e.g. von Frese *et al.* 1981a,b; Dyment & Arkani-Hamed 1998a; Langel & Hinze 1998; von Frese 1998) or Green's function (e.g. Parker *et al.* 1987; Whaler & Langel 1996) and the tesseroids (e.g. Asgharzadeh *et al.* 2008). These methods, especially in the space domain, have been widely used. For examples, forward modelling (e.g. Dyment & Arkani-Hamed 1998b; Hemant & Maus 2005; Masterton *et al.* 2013), inverse modelling (e.g. Whaler & Langel 1996; Purucker *et al.* 1998, 2002; Whaler & Purucker 2005; Carley *et al.* 2012), surface heat flux modelling (e.g. Fox Maule *et al.* 2005), magnetic field transformations, such as altitude normalization, spatial derivatives, continuations, pseudo-gravity anomaly and differential magnetic pole reductions (e.g. von Frese *et al.* 1981b, 1982; Purucker *et al.* 2000; Asgharzadeh *et al.* 2008). Such methods are available for satellite altitudes, but for the calculation at a low altitude, for example downward continuation (e.g. Whaler 1994), joint modelling with surface data or aeromagnetic data (e.g. Kim *et al.* 2013), and also the 3-D inversion for lithospheric magnetization structure (e.g. Du *et al.* 2013, 2014), an efficient forward modelling algorithm to calculate the magnetic effects for any observation point outside the Earth caused by regionally or locally magnetized bodies in the SCS is particularly necessary (e.g. von Frese *et al.* 1981a; Lane 2009).

Being similar to the rectangular prism (RP) in the Cartesian coordinate system (CCS), as a simple and popular approach, the tesseroid is the best choice for the basic magnetized element in the SCS. According to Anderson (1976), the tesseroid is bounded by geographic grid lines and surfaces of constant ellipsoidal height. Generally, the ellipsoidal body is approximated by corresponding spherical prism (SP), which is bounded by geocentric spherical coordinates. Even though spherical tesseroids are considered in the following, the Earth's ellipticity can be taken into account by fixing these bodies on an ellipsoidal reference surface with a latitude-dependent Earth radius (e.g. Heck & Seitz 2007). However, there is no analytic solution for the tesseroid in the SCS (e.g. Grüninger 1990). Therefore, many approximate solutions have been proposed. For example, the Gauss–Legendre quadrature integration method (GLQI) is utilized to forward model the magnetic effects of the SP in the SCS (von Frese *et al.* 1981a,b; Asgharzadeh *et al.* 2008).

In contrast, the gravity effects of the tesseroid in the SCS have been widely studied. Heck & Seitz (2007) and Wild-Pfeiffer (2008) derived the fourth-order approximations which applied the Taylor's series expansion (TSE) of the integral kernel. While Heck & Seitz (2007) originally derived formulas for the tesseroid potential and the first radial derivative, and Wild-Pfeiffer (2007, 2008) extended the approach to all components of first- and second-order derivatives. Furthermore, also Gauss–Legendre cubature is applied to gravity and its gradient fields proposed by Asgharzadeh *et al.* (2007) and Wild-Pfeiffer (2007, 2008). For global computations, another alternative consists of analytically solving the 1-D integral with respect to the geocentric distance and calculating the remaining 2-D surface integral numerically (e.g. Martinec 1998; Heck & Seitz 2007). Especially, Grombein *et al.* (2010, 2013) derived the new tesseroid formulas based on the Cartesian integral kernels but not the spherical integral kernels. The optimized formulas allow an efficient numerical evaluation with a significantly reduced runtime and the polar singularity is also overcome. Alternatively, Lane (2009) used a set of the equivalent point masses as approximation of the SP to compute the vertical gravity and its vertical gradient and investigate the differences between the fields by the SP in the spherical frame and by the RP in the Cartesian frame. The results show that the differences become larger as the computing points far away the sources.

In this study, based on the work in the gravity field, we present three kinds of forward modelling methods for the magnetic effects (i.e. magnetic potential, vector and gradient tensor fields) caused by the tesseroid in the geocentric SCS. First, in Section 2, we give the optimized formulas by the TSE, the revised Gauss–Legendre quadrature integration (RGLQI) and the frame of approximations by Cartesian elements. Then, in Section 3, the subdivision technique and the necessary transforms of coordinates and fields in different coordinate systems are introduced. In Section 4, we analyse the accuracies and computational efficiencies of all methods. Besides, as an actual numerical example, the magnetic potential, vector and gradient tensor fields are computed globally using tesseroids by the 3-D RGLQI on the basis of a global vertical integrated magnetization (VIM) vector model of the Earth's lithosphere. At last, in Section 5, discussion and some conclusions are given and main topics of future work about this issue are also suggested.

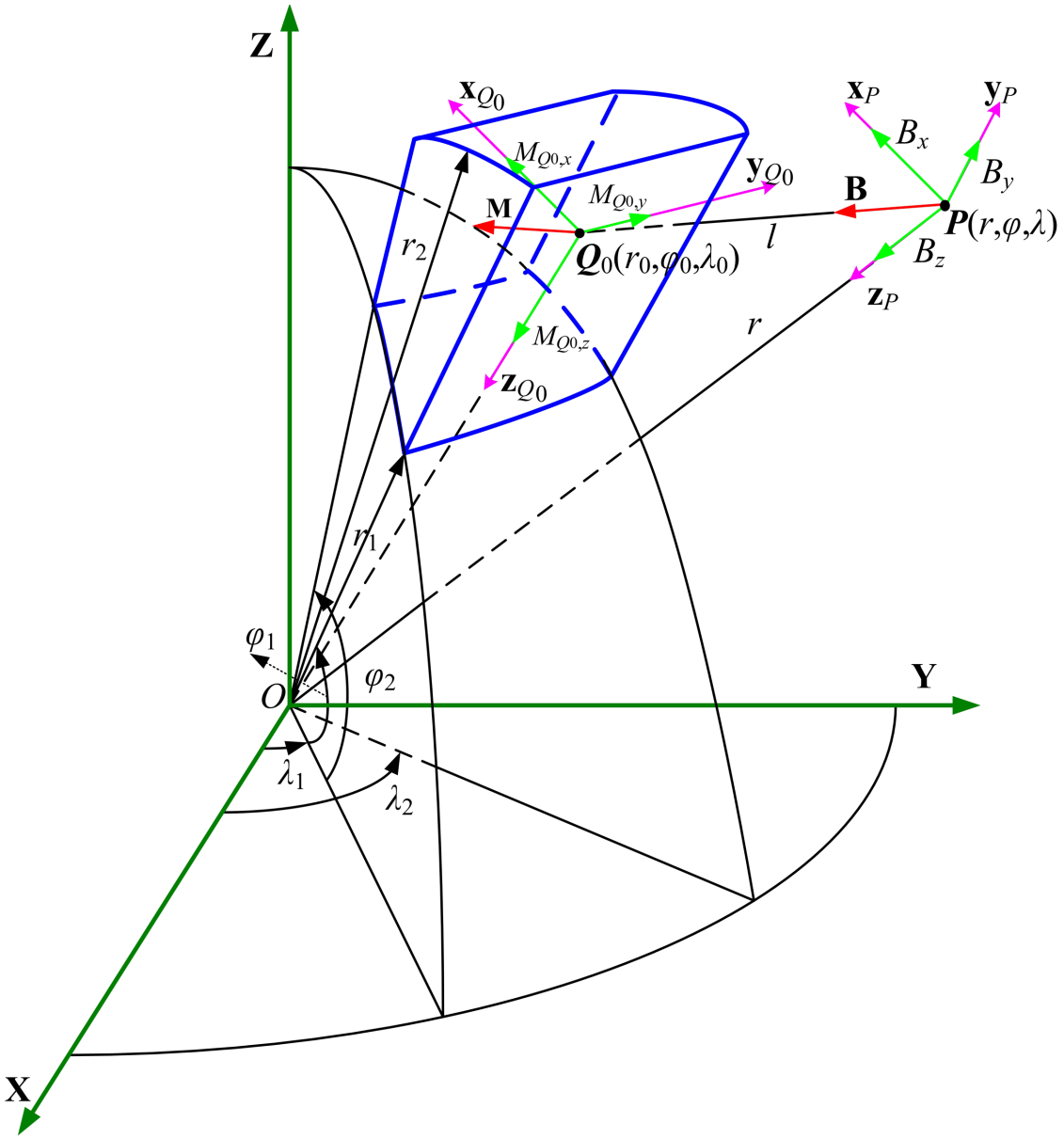

Figure 1. Geometry of the tesseroid and view of the spherical source-centred local CCS ($\mathbf{x}_Q, \mathbf{y}_Q, \mathbf{z}_Q$), spherical observation-centred local CCS ($\mathbf{x}_P, \mathbf{y}_P, \mathbf{z}_P$), global geocentric SCS ($\mathbf{r}, \boldsymbol{\varphi}, \boldsymbol{\lambda}$) and global geocentric CCS ($\mathbf{X}, \mathbf{Y}, \mathbf{Z}$). Q_0 is the geometric centre of the tesseroid, and r, φ and λ are the radius, latitude and longitude, respectively.

2 METHODOLOGY

In Section 2.1 the tesseroid and the required coordinate systems are introduced, while Section 2.2 focuses on the basic formulas for the magnetic potential and its partial derivatives. Then in Sections 2.3–2.5, the optimized formulas by the 3-D TSE, the 3-D RGLQI approaches and the approximations by Cartesian elements are presented, respectively.

2.1 Tesseroid and coordinate systems

The RP, the most common cell, is often used in the forward modelling, inversion and interpretation in CCS. Alternatively, in the geocentric SCS, the SP or so-called the tesseroid (e.g. Anderson 1976; Heck & Seitz 2007; Fig. 1), is chosen as basic element for forward modelling, which is bounded by (i) a pair of surfaces with the constant spherical radius $r_1 = \text{const}$, $r_2 = \text{const}$, that are 'parallel' to the reference sphere; (ii) a pair of meridional planes with $\lambda_1 = \text{const}$, $\lambda_2 = \text{const}$ and (iii) a pair of coaxial circular cones ($\varphi_1 = \text{const}$, $\varphi_2 = \text{const}$). The point $Q_0(r_0, \varphi_0, \lambda_0)$ is the geometric centre of the tesseroid, where $r_0 = (r_1 + r_2)/2$, $\varphi_0 = (\varphi_1 + \varphi_2)/2$ and $\lambda_0 = (\lambda_1 + \lambda_2)/2$.

We first define the spherical source-centred CCS ($\mathbf{x}_Q, \mathbf{y}_Q, \mathbf{z}_Q$) to describe the magnetization vector $\mathbf{M}_Q(r', \varphi', \lambda')$ for the tesseroid (Fig. 1), where the $Q(r', \varphi', \lambda')$ denotes any point inside the magnetic source. The $\mathbf{x}_Q$-axis of the right-handed system as used in the following points

north, the $\mathbf{y}_Q$-axis points east, and the $\mathbf{z}_Q$-axis points towards into the geocentric radial direction. Thus, the magnetization vector can be expressed as:

$$\mathbf{M}_Q = \mathrm{M}_{Q,x}\mathbf{x}_Q + \mathrm{M}_{Q,y}\mathbf{y}_Q + \mathrm{M}_{Q,z}\mathbf{z}_Q, \tag{1}$$

where $\mathbf{x}_Q$, $\mathbf{y}_Q$, $\mathbf{z}_Q$ are the unit vectors in the spherical source-centred CCS.

We then define the spherical observation-centred CCS to describe the magnetic effects by the tesseroid (Fig. 1). This CCS ($\mathbf{x}_P, \mathbf{y}_P, \mathbf{z}_P$) is located at the observation point $P(r, \varphi, \lambda)$. The $\mathbf{x}_P$-axis of the right-handed system as used in the following points north, the $\mathbf{y}_P$-axis points east and the $\mathbf{z}_P$-axis points towards into the geocentric radial direction. Thus, the magnetic vector $\mathbf{B} = -\nabla V$ and the complete gradient tensor $\nabla\mathbf{B}$ can be expressed as:

$$\mathbf{B} = B_{\mathrm{x}}\mathbf{x}_P + B_y\mathbf{y}_P + B_z\mathbf{z}_P = (-\partial V/\partial \mathrm{x}_P\mathbf{x}_P) + (-\partial V/\partial \mathrm{y}_P\mathbf{y}_P) + (-\partial V/\partial z_P\mathbf{z}_P), \tag{2}$$

$$\nabla\mathbf{B} = \begin{bmatrix} B_{\mathrm{xx}} & B_{\mathrm{xy}} & B_{\mathrm{xz}} \\ B_{\mathrm{yx}} & B_{\mathrm{yy}} & B_{\mathrm{yz}} \\ B_{\mathrm{zx}} & B_{\mathrm{zy}} & B_{\mathrm{zz}} \end{bmatrix} = \begin{bmatrix} -\partial^2 V/\partial \mathrm{x}_P\partial \mathrm{x}_P & -\partial^2 V/\partial \mathrm{x}_P\partial \mathrm{y}_P & -\partial^2 V/\partial \mathrm{x}_P\partial \mathrm{z}_P \\ -\partial^2 V/\partial \mathrm{y}_P\partial \mathrm{x}_P & -\partial^2 V/\partial \mathrm{y}_P\partial \mathrm{y}_P & -\partial^2 V/\partial \mathrm{y}_P\partial \mathrm{z}_P \\ -\partial^2 V/\partial \mathrm{z}_P\partial \mathrm{x}_P & -\partial^2 V/\partial \mathrm{z}_P\partial \mathrm{y}_P & -\partial^2 V/\partial \mathrm{z}_P\partial \mathrm{z}_P \end{bmatrix}, \tag{3}$$

where $\mathbf{x}_P$, $\mathbf{y}_P$, $\mathbf{z}_P$ are the unit vectors in the spherical observation-centred CCS and V is the magnetic scalar potential. Since in source-free space the magnetic potential field is irrotational, that is $\nabla \times (\nabla V) = 0$, and the potential is a harmonic function outside the tesseroid, the Marussi tensor is symmetric and trace-free due to the Laplace equation, that is $B_{\mathrm{xx}} + B_{\mathrm{yy}} + B_{\mathrm{zz}} = 0$, therefore, only five out of nine elements are independent.

2.2 Basic formulas

The magnetic potential $V(r, \varphi, \lambda)$ of a magnetized element with magnetization vector $\mathbf{M}_Q(r', \varphi', \lambda')$ can be described as (e.g. Blakely 1995)

$$V(r, \varphi, \lambda) = \frac{\mu_0}{4\pi}\int_{\Omega} \mathbf{M}_Q(r', \varphi', \lambda') \cdot \nabla_Q \frac{1}{l}\,\mathrm{d}\Omega, \tag{4}$$

where $l = l(P, Q) = \sqrt{r^2 + r'^2 - 2rr'\cos\psi}$ denotes the Euclidean distance function between the computational point $P(r, \varphi, \lambda) \notin \Omega$ and the running integration point $Q(r', \varphi', \lambda') \in \Omega$. $\Omega := [r_1, r_2] \times [\varphi_1, \varphi_2] \times [\lambda_1, \lambda_2] \subset \mathrm{R}^3$ is the integration domain. $\mathrm{d}\Omega = r'^2\cos\varphi'\mathrm{d}r'\mathrm{d}\varphi'\mathrm{d}\lambda'$ is the spherical volume element and μ_0 is the permeability ($4\pi \times 10^{-7}\mathrm{N}\cdot\mathrm{A}^{-2}$). The spherical angle distance ψ between the position vectors of $P(\mathbf{r})$ and $Q(\mathbf{r}')$ is given by

$$\cos\psi(P, Q) = \sin\varphi\sin\varphi' + \cos\varphi\cos\varphi'\cos(\lambda' - \lambda). \tag{5}$$

According to Grombein *et al.* (2013), the Cartesian coordinates of the running integration point Q in the observation-centred CCS can be expressed as:

$$x' = r'\sin\psi\cos\alpha, \tag{6a}$$

$$y' = r'\sin\psi\sin\alpha, \tag{6b}$$

$$z' = r - r'\cos\psi, \tag{6c}$$

where α denotes the azimuth angle at $P(\mathbf{r})$ in direction to $Q(\mathbf{r}')$. Based on the relations of spherical trigonometry (e.g. Heiskanen & Moritz 1967)

$$\sin\psi\cos\alpha = \cos\varphi\sin\varphi' - \sin\varphi\cos\varphi'\cos(\lambda' - \lambda), \tag{7a}$$

$$\sin\psi\sin\alpha = \cos\varphi'\sin(\lambda' - \lambda), \tag{7b}$$

therefore, eq. (6) can be written as:

$$x' = r'\left[\cos\varphi\sin\varphi' - \sin\varphi\cos\varphi'\cos(\lambda' - \lambda)\right], \tag{8a}$$

$$y' = r'\cos\varphi'\sin(\lambda' - \lambda), \tag{8b}$$

$$z' = r - r'\cos\psi. \tag{8c}$$

By making use of the derived functional relations in eq. (8), the Euclidean distance between P and Q can be expressed in the spherical observation-centred CCS by

$$l(P, Q) = \sqrt{x'^2 + y'^2 + z'^2}. \tag{9}$$

In the spherical observation point P-centred CCS, eq. (4) can be expressed as:

$$V(r, \varphi, \lambda) = \frac{\mu_0}{4\pi} \int_\Omega \mathbf{M}_P\left(r', \varphi', \lambda'\right) \cdot \nabla_Q \frac{1}{\sqrt{x'^2 + y'^2 + z'^2}} \mathrm{d}\Omega, \tag{10}$$

where $\mathbf{M}_P(r', \varphi', \lambda') = \mathbf{R}(r, \varphi, \lambda, r', \varphi', \lambda')[\mathbf{M}_Q(r', \varphi', \lambda')]$ is the magnetization vector expressed in the spherical observation-centred CCS (the transformation matrix $\mathbf{R}$ will be given in Section 3.2) and the term of ∇_Q is also operated in the spherical observation-centred CCS. Asgharzadeh *et al.* (2008) introduced the angle β between the magnetization vector and the gradient tensor of the $1/l$ in the geocentric CCS to express the magnetic potential as:

$$V(r, \varphi, \lambda) = \frac{\mu_0}{4\pi} \int_\Omega -|\mathbf{M}| \frac{\cos\beta}{l^2} \mathrm{d}\Omega. \tag{11}$$

According to the definition of the spherical source-centred CCS for the magnetization vector $\mathbf{M}$, a homogeneous magnetization means that the amplitude of the $\mathbf{M}$ is constant but also the directions of the $\mathbf{M}$, those are the magnetized inclination I and declination D, are actually variable in a fixed CCS. In this case, the problem becomes complicated. In fact, for a SP with a general geometric scale in a fixed CCS, such as $0.5^\circ \times 0.5^\circ$ on spherical surface, relative to the direction of the $\mathbf{M}$ in the geometric centre of the SP, the maximum variation of the directions is 0.25°, the difference between the $\cos(\beta + 0.25^\circ)$ and the $\cos\beta$ is so small that can be ignored. Especially, with the aid of the subdivision, which will be presented in Section 3.1, will make the difference much smaller. Therefore, to simplify the forward problem, the homogeneous magnetization vector is approximated by the vector at the geometric centre $Q_0(r_0, \varphi_0, \lambda_0)$ of the SP. Thus, the eq. (10) can be written as:

$$V(r, \varphi, \lambda) = \frac{\mu_0}{4\pi} \int_\Omega \mathbf{M}_P(r_0, \varphi_0, \lambda_0) \cdot \nabla_Q \frac{1}{\sqrt{x'^2 + y'^2 + z'^2}} \mathrm{d}\Omega. \tag{12}$$

Further, assuming the $i, j, k = 1, 2, 3$ denote x, y and z, respectively, and assuming the x_1, x_2 and x_3 denote x', y' and z', respectively, the magnetic effects can be expressed as:

$$V(r, \varphi, \lambda) = \frac{\mu_0}{4\pi} \int_\Omega \sum_{i=1}^{3} M_{P,i}(r_0, \varphi_0, \lambda_0)\, T_i \mathrm{d}\Omega, \tag{13}$$

and

$$T_i = \frac{1}{l} \cdot \left(-\frac{x_i}{l^2}\right). \tag{14}$$

In the spherical observation-centred CCS, $\nabla_P V$ is equivalent to $-\nabla_Q V$ and $\nabla_P \mathbf{B}$ is equivalent to $-\nabla_Q \mathbf{B}$ based on the eq. (8) and the eq. (12). Therefore, according to eqs (2) and (3), the magnetic vector $\mathbf{B}$ and the complete gradient tensor $\nabla\mathbf{B}$ can be expressed as:

$$B_i(r, \varphi, \lambda) = \frac{\mu_0}{4\pi} \int_\Omega \sum_{j=1}^{3} M_{P,j}(r_0, \varphi_0, \lambda_0)\, T_{ij} \mathrm{d}\Omega, \tag{15}$$

$$B_{ij}(r, \varphi, \lambda) = \frac{\mu_0}{4\pi} \int_\Omega \sum_{k=1}^{3} M_{P,k}(r_0, \varphi_0, \lambda_0)\, T_{kij} \mathrm{d}\Omega, \tag{16}$$

and

$$T_{ij} = \frac{1}{l^3}\left(\frac{3x_i x_j}{l^2} - \delta_{ij}\right), \tag{17}$$

$$T_{kij} = \frac{1}{l^5}\left[\frac{15x_i x_j x_k}{l^2} - 3x_k\left(\delta_{ij} + \delta_{ki} + \delta_{kj}\right)\right], \tag{18}$$

where δ_{ij}, δ_{ki} and δ_{kj} denote the Kronecker delta functions, taking the δ_{ij} for example, $\delta_{ij} = 1$ if $i = j$ and $\delta_{ij} = 0$ otherwise.

In eqs (13), (15) and (16), these formulas comprise elliptic integrals that have to be evaluated numerically. If considering the Earth's ellipticity, the radii r_1 and r_2 of the lower surface and the upper surface can be replaced, roughly by the surfaces with geocentric latitude-dependent Earth's radii of the reference ellipsoid in the geocentric SCS, or more preferably by the surfaces with geographic latitude-dependent Earth's radii in the geographic SCS (e.g. Heck & Seitz 2007) where some extra transformations for the coordinates and the magnetic effects are required. Providing the magnetic effects are expressed in the ellipsoidal local CCS, the magnetic vector and its tensor should be rotated on the $\mathbf{y}_P$ axis further because of the difference between the geocentric latitude and the geographic latitude.

2.3 Taylor's series expansion

Equivalently to Heck & Seitz (2007) and Grombein *et al.* (2013), we integrate the TSE of the Cartesian integral kernels in eqs (13), (15) and (16) at the tesseroid's geometrical centre point $Q_0(r_0, \varphi_0, \lambda_0)$, where the magnetization vector is treated as a constant vector. Here because the terms of odd order and mixed terms in the Taylor's series vanish after integration, the corresponding integrals can be expanded as:

$$\left\{\begin{array}{l}\int_\Omega T_i \mathrm{d}\Omega \\ \int_\Omega T_{ij} \mathrm{d}\Omega \\ \int_\Omega T_{kij} \mathrm{d}\Omega\end{array}\right\} = \Delta r \Delta\varphi \Delta\lambda \left\{\begin{array}{l}K_i(P,Q) \\ L_{ij}(P,Q) \\ N_{kij}(P,Q)\end{array}\right\} \left| \begin{array}{l} r' = r_0 \\ \varphi' = \varphi_0 \\ \lambda' = \lambda_0 \end{array}\right.$$

$$+\frac{\Delta r \Delta\varphi \Delta\lambda}{24} \left\{\begin{array}{l}(\Delta r)^2 \partial^2_{r'} K_i(P,Q) + (\Delta\varphi)^2 \partial^2_{\varphi'} K_i(P,Q) + (\Delta\lambda)^2 \partial^2_{\lambda'} K_i(P,Q) \\ (\Delta r)^2 \partial^2_{r'} L_{ij}(P,Q) + (\Delta\varphi)^2 \partial^2_{\varphi'} L_{ij}(P,Q) + (\Delta\lambda)^2 \partial^2_{\lambda'} L_{ij}(P,Q) \\ (\Delta r)^2 \partial^2_{r'} N_{kij}(P,Q) + (\Delta\varphi)^2 \partial^2_{\varphi'} N_{kij}(P,Q) + (\Delta\lambda)^2 \partial^2_{\lambda'} N_{kij}(P,Q)\end{array}\right\} \left| \begin{array}{l} r' = r_0 \\ \varphi' = \varphi_0 \\ \lambda' = \lambda_0 \end{array}\right.$$

$$+\left\{\begin{array}{l}O\left[\Delta^4/l^6(P,Q_0)\right] \\ O\left[\Delta^4/l^7(P,Q_0)\right] \\ O\left[\Delta^4/l^8(P,Q_0)\right]\end{array}\right\}, \tag{19}$$

where $\Delta r = r_2 - r_2$, $\Delta\varphi = \varphi_2 - \varphi_1$ and $\Delta\lambda = \lambda_2 - \lambda_1$, and $O[\Delta^4]$ indicates that terms of fourth-order and higher terms in Δr, $\Delta\varphi$ and $\Delta\lambda$ are omitted. The term of zero-order is

$$\left\{\begin{array}{l}K_i(P,Q) \\ L_{ij}(P,Q) \\ N_{kij}(P,Q)\end{array}\right\} = \frac{1}{l^3} \left\{\begin{array}{l}-x_i \\ \dfrac{3x_i x_j}{l^2} - \delta_{ij} \\ \dfrac{15x_i x_j x_k}{l^4} + \dfrac{3\left(\delta_{ijk} - x_k \delta_{ij}\right)}{l^2}\end{array}\right\} \tau, \tag{20}$$

where $\tau = r'^2 \cos\varphi'$ factors the spherical volume element $\mathrm{d}\Omega$. While the required second-order derivatives in eq. (19) can be represented in the general form as

$$\left\{\begin{array}{l}\partial^2_m K_i(P,Q) \\ \partial^2_m L_{ij}(P,Q) \\ \partial^2_m N_{kij}(P,Q)\end{array}\right\} = \left\{\begin{array}{l}\left(\partial^2_m K_u\right) K_v + 2\left(\partial_m K_u\right)\left(\partial_m K_v\right) + K_u\left(\partial^2_m K_v\right) \\ \left(\partial^2_m K_u\right) L_v + 2\left(\partial_m K_u\right)\left(\partial_m L_v\right) + K_u\left(\partial^2_m L_v\right) \\ \left(\partial^2_m K_u\right) N_v + 2\left(\partial_m K_u\right)\left(\partial_m N_v\right) + K_u\left(\partial^2_m N_v\right)\end{array}\right\}, \qquad m = r', \varphi', \lambda', \tag{21}$$

where the detailed expressions in eq. (21) are presented in Appendix A. Inserting these expressions into eq. (21) and then inserting eqs (21) and (20) into eq. (19), at last inserting eq. (19) into eqs (13), (15) and (16), the magnetic potential, vector and gradient tensor fields of the tesseroid can be calculated approximately. In theory, modelling error by the TSE depends on the approximation of the magnetization's direction and also the truncation terms. If the subdivision given in Section 3.1 is applied, these two kinds of errors will be both suppressed. Besides, the truncated terms l^{-6}, l^{-7} and l^{-8} for V, B_i and B_{ij} in eq. (19), respectively, suggest that as l increasing the error of V decays most slowly and most quickly for B_{ij}.

2.4 3-D Gauss–Legendre quadrature integration

Based on the eq. (13), eq. (15) and eq. (16), the magnetic potential, vector and gradient tensor fields caused by the tesseroid can be expressed as

$$V = \frac{\mu_0}{4\pi} \int_{\lambda_1}^{\lambda_2} \int_{\varphi_1}^{\varphi_2} \int_{r_1}^{r_2} f_V \mathrm{d}r' \mathrm{d}\varphi' \mathrm{d}\lambda', \tag{22}$$

$$B_i = \frac{\mu_0}{4\pi} \int_{\lambda_1}^{\lambda_2} \int_{\varphi_1}^{\varphi_2} \int_{r_1}^{r_2} f_{B_i} \mathrm{d}r' \mathrm{d}\varphi' \mathrm{d}\lambda', \tag{23}$$

$$B_{ij} = \frac{\mu_0}{4\pi} \int_{\lambda_1}^{\lambda_2} \int_{\varphi_1}^{\varphi_2} \int_{r_1}^{r_2} f_{B_{ij}} \mathrm{d}r' \mathrm{d}\varphi' \mathrm{d}\lambda', \tag{24}$$

where $i, j = x, y, z$, and the integrals are, respectively, as

$$f_V\left(r,\varphi,\lambda,r',\varphi',\lambda'\right)=\tau\sum_{i=1}^{3}M_{P,i}\left(r',\varphi',\lambda'\right)T_i, \tag{25}$$

$$f_{B_i}\left(r,\varphi,\lambda,r',\varphi',\lambda'\right)=\tau\sum_{j=1}^{3}M_{P,j}\left(r',\varphi',\lambda'\right)T_{ij}, \tag{26}$$

$$f_{B_{ij}}\left(r,\varphi,\lambda,r',\varphi',\lambda'\right)=\tau\sum_{k=1}^{3}M_{P,k}\left(r',\varphi',\lambda'\right)T_{kij}. \tag{27}$$

Note here at each Gaussian point, the magnetization vector should be first transformed from the spherical source-centred CCS to the spherical observation-centred CCS. According to the GLQI decomposition (Stroud & Secrest 1966; Ku 1977; von Frese *et al.* 1981a; Asgharzadeh *et al.* 2007, 2008; Wild-Pfeiffer 2008; Grombein *et al.* 2010; Li *et al.* 2011), the integrals in eqs (22)–(24) have the least squares numerical solutions as

$$V=\frac{\mu_0}{4\pi}\frac{(r_2-r_1)(\varphi_2-\varphi_1)(\lambda_2-\lambda_1)}{8}\sum_{n_r=0}^{L}\sum_{n_\varphi=0}^{M}\sum_{n_\lambda=0}^{N}A_{n_r}A_{n_\varphi}A_{n_\lambda}f_V\left(r,\varphi,\lambda,\hat{r}_{n_r},\hat{\varphi}_{n_\varphi},\hat{\lambda}_{n_\lambda}\right), \tag{28}$$

$$B_i=\frac{\mu_0}{4\pi}\frac{(r_2-r_1)(\varphi_2-\varphi_1)(\lambda_2-\lambda_1)}{8}\sum_{n_r=0}^{L}\sum_{n_\varphi=0}^{M}\sum_{n_\lambda=0}^{N}A_{n_r}A_{n_\varphi}A_{n_\lambda}f_{B_i}\left(r,\varphi,\lambda,\hat{r}_{n_r},\hat{\varphi}_{n_\varphi},\hat{\lambda}_{n_\lambda}\right), \tag{29}$$

$$B_{ij}=\frac{\mu_0}{4\pi}\frac{(r_2-r_1)(\varphi_2-\varphi_1)(\lambda_2-\lambda_1)}{8}\sum_{n_r=0}^{L}\sum_{n_\varphi=0}^{M}\sum_{n_\lambda=0}^{N}A_{n_r}A_{n_\varphi}A_{n_\lambda}f_{B_{ij}}\left(r,\varphi,\lambda,\hat{r}_{n_r},\hat{\varphi}_{n_\varphi},\hat{\lambda}_{n_\lambda}\right), \tag{30}$$

where the Gauss–Legendre coefficients $(A_{n_r}, A_{n_\varphi}, A_{n_\lambda})$ are functions of the coordinates $(\hat{r}_{n_r}, \hat{\varphi}_{n_\varphi}, \hat{\lambda}_{n_\lambda})$ of the (n_rth, n_φth, n_λth) Gaussian node with maximum (L, M, N) in the open interval $(-1, +1)$. Each node is the coordinate for a zero of the nth order Legendre polynomial that orthogonally spans the unit interval. In the application (e.g. eqs 28–30), however, the nodes must be scaled to the actual coordinates $(r_{n_r}, \varphi_{n_\varphi}, \lambda_{n_\lambda})$ within the tesseroid by

$$r_{n_r}=\frac{\hat{r}_{n_r}(r_2-r_1)+(r_2+r_1)}{2}, \tag{31a}$$

$$\varphi_{n_\varphi}=\frac{\hat{\varphi}_{n_\varphi}(\varphi_2-\varphi_1)+(\varphi_2+\varphi_1)}{2}, \tag{31b}$$

$$\lambda_{n_\lambda}=\frac{\hat{\lambda}_{n_\lambda}(\lambda_2-\lambda_1)+(\lambda_2+\lambda_1)}{2}. \tag{31c}$$

These expressions, such as the eqs (25)–(27), are relatively simple compared with the formulas derived by Asgharzadeh *et al.* (2008). The remaining issue is to select an appropriate number of Gaussian nodes so that a better result is obtained in an acceptable time. The studies by Ku (1977) and von Frese *et al.* (1981a) show that the error of the solution remains essentially unchanged for different numbers of nodes as long as the node spacing is smaller than the distance to the observing point. However, purely increasing the number of the Gaussian nodes will result into a time-consuming process, and aspect of computational efficiency will be discussed further in Section 4.

2.5 Approximations by Cartesian elements

In this section, we employ the Cartesian elements with same volume to approximate the tesseroid. There are many kinds of the traditional Cartesian elements, such as the point, sphere, ellipsoid, RP, layer, line and vertical cylinder etc., but in this study we just present the popular methods of the magnetic dipole (MD) and the RP.

In the spherical source-centred CCS defined in Section 2.1, the magnetic effects at any observation point $P(\mathrm{x}_Q,\mathrm{y}_Q,\mathrm{z}_Q)$ by the MD point $Q(\xi, \eta, \zeta)$ can be expressed as:

$$V=\frac{\mu_0}{4\pi}\left(\frac{\mathbf{m}\cdot\mathbf{r}}{r^3}\right), \tag{32}$$

$$B_i=\frac{\mu_0}{4\pi}\left[\frac{3(\mathbf{m}\cdot\mathbf{r})r_i}{r^5}-\frac{m_i}{r^3}\right], \tag{33}$$

$$B_{ij}=\frac{\mu_0}{4\pi}\left[\frac{-15\mathbf{m}\cdot\mathbf{r}}{r^7}ij+\frac{3m_i\cdot j}{r^5}+\frac{3m_j\cdot i}{r^5}+\frac{3\delta_{ij}(\mathbf{m}\cdot\mathbf{r})}{r^5}\right], \tag{34}$$

where the magnetic moment $\mathbf{m}=\mathbf{M}_Q\cdot\Omega$, $\mathbf{r}=(x_Q-\xi)\mathbf{x}_Q+(y_Q-\eta)\mathbf{y}_Q+(z_Q-\zeta)\mathbf{z}_Q$, $r=\|\mathbf{r}\|$ is the Euler distance between the points $P(\mathrm{x}_Q,\mathrm{y}_Q,\mathrm{z}_Q)$ and $Q(\xi, \eta, \zeta)$, and the accurate volume of the tesseroid is $\Omega=\frac{1}{3}(r_2^3-r_1^3)(\sin\varphi_2-\sin\varphi_1)(\lambda_2-\lambda_1)$, and $i, j=x, y, z$.

Providing the sides of the RP are parallel to the three Cartesian coordinate axis, the magnetic effects at any observation point $P(x_Q,y_Q,z_Q)$ by the RP whose geometric centre is $Q\,(\xi,\eta,\zeta)$ can be expressed as:

$$V = \frac{\mu_0}{4\pi}\left(M_{Q,x}A_x + M_{Q,y}A_y + M_{Q,z}A_z\right)\Big|_{\xi-a/2}^{\xi+a/2}\Big|_{\eta-b/2}^{\eta+b/2}\Big|_{\zeta-c/2}^{\zeta+c/2}, \tag{35}$$

$$B_x = \frac{\mu_0}{4\pi}\left(M_{Q,x}A_{xx} + M_{Q,y}A_{xy} + M_{Q,z}A_{xz}\right)\Big|_{\xi-a/2}^{\xi+a/2}\Big|_{\eta-b/2}^{\eta+b/2}\Big|_{\zeta-c/2}^{\zeta+c/2}, \tag{36a}$$

$$B_y = \frac{\mu_0}{4\pi}\left(M_{Q,x}A_{yx} + M_{Q,y}A_{yy} + M_{Q,z}A_{yz}\right)\Big|_{\xi-a/2}^{\xi+a/2}\Big|_{\eta-b/2}^{\eta+b/2}\Big|_{\zeta-c/2}^{\zeta+c/2}, \tag{36b}$$

$$B_z = \frac{\mu_0}{4\pi}\left(M_{Q,x}A_{zx} + M_{Q,y}A_{zy} + M_{Q,z}A_{zz}\right)\Big|_{\xi-a/2}^{\xi+a/2}\Big|_{\eta-b/2}^{\eta+b/2}\Big|_{\zeta-c/2}^{\zeta+c/2}, \tag{36c}$$

$$B_{xx} = \frac{\mu_0}{4\pi}\left(M_{Q,x}A_{xxx} + M_{Q,y}A_{xyx} + M_{Q,z}A_{xzx}\right)\Big|_{\xi-a/2}^{\xi+a/2}\Big|_{\eta-b/2}^{\eta+b/2}\Big|_{\zeta-c/2}^{\zeta+c/2}, \tag{37a}$$

$$B_{xy} = B_{yx} = \frac{\mu_0}{4\pi}\left(M_{Q,x}A_{xxy} + M_{Q,y}A_{xyy} + M_{Q,z}A_{xzy}\right)\Big|_{\xi-a/2}^{\xi+a/2}\Big|_{\eta-b/2}^{\eta+b/2}\Big|_{\zeta-c/2}^{\zeta+c/2}, \tag{37b}$$

$$B_{xz} = B_{zx} = \frac{\mu_0}{4\pi}\left(M_{Q,x}A_{xxz} + M_{Q,y}A_{xyz} + M_{Q,z}A_{xzz}\right)\Big|_{\xi-a/2}^{\xi+a/2}\Big|_{\eta-b/2}^{\eta+b/2}\Big|_{\zeta-c/2}^{\zeta+c/2}, \tag{37c}$$

$$B_{yy} = \frac{\mu_0}{4\pi}\left(M_{Q,x}A_{yxy} + M_{Q,y}A_{yyy} + M_{Q,z}A_{yzy}\right)\Big|_{\xi-a/2}^{\xi+a/2}\Big|_{\eta-b/2}^{\eta+b/2}\Big|_{\zeta-c/2}^{\zeta+c/2}, \tag{37d}$$

$$B_{yz} = B_{zy} = \frac{\mu_0}{4\pi}\left(M_{Q,x}A_{yxz} + M_{Q,y}A_{yyz} + M_{Q,z}A_{yzz}\right)\Big|_{\xi-a/2}^{\xi+a/2}\Big|_{\eta-b/2}^{\eta+b/2}\Big|_{\zeta-c/2}^{\zeta+c/2}, \tag{37e}$$

$$B_{zz} = \frac{\mu_0}{4\pi}\left(M_{Q,x}A_{zxz} + M_{Q,y}A_{zyz} + M_{Q,z}A_{zzz}\right)\Big|_{\xi-a/2}^{\xi+a/2}\Big|_{\eta-b/2}^{\eta+b/2}\Big|_{\zeta-c/2}^{\zeta+c/2}, \tag{37f}$$

where the detailed expressions for A_i, A_{ij} and A_{ijk}, $i, j, k = x, y, z$ are presented in Appendix B; $r = \sqrt{(\xi' - x_Q)^2 + (\eta' - y_Q)^2 + (\zeta' - z_Q)^2}$ in the Appendix B is the Euclidean distance between computing point and integrating point; a, b and c are the length of sides in $\mathbf{x}_Q$, $\mathbf{y}_Q$ and $\mathbf{z}_Q$ directions of the RP and the lengths can be calculated by the 'equivalent volume' RP defined by Heck & Seitz (2007) as:

$$a = r_0\,(\varphi_2 - \varphi_1)\,, \tag{38a}$$

$$b = r_0 \cos\varphi_0\,(\lambda_2 - \lambda_1)\,, \tag{38b}$$

$$c = r_2 - r_1. \tag{38c}$$

Note that all the points, magnetization vector and gradient tensor are expressed in the spherical source-centred CCS. These mean that in any observing point $P(r, \varphi, \lambda)$, we should first translate the coordinates from the geocentric spherical coordinates (r, φ, λ) to the spherical source-centred Cartesian coordinates $(\mathbf{x}_Q, \mathbf{y}_Q, \mathbf{z}_Q)$ and then translate the calculated magnetic effects from the spherical source-centred CCS to the spherical observation-centred CCS (the transformations will be presented in Section 3.2). The solutions by the Cartesian elements are analytical and thus the computational accuracy only depends on the geometric approximation to the tesseroid and also the approximation of the magnetization's direction. However, adopting the subdividing technique (Section 3.1), both two kinds of errors will be suppressed.

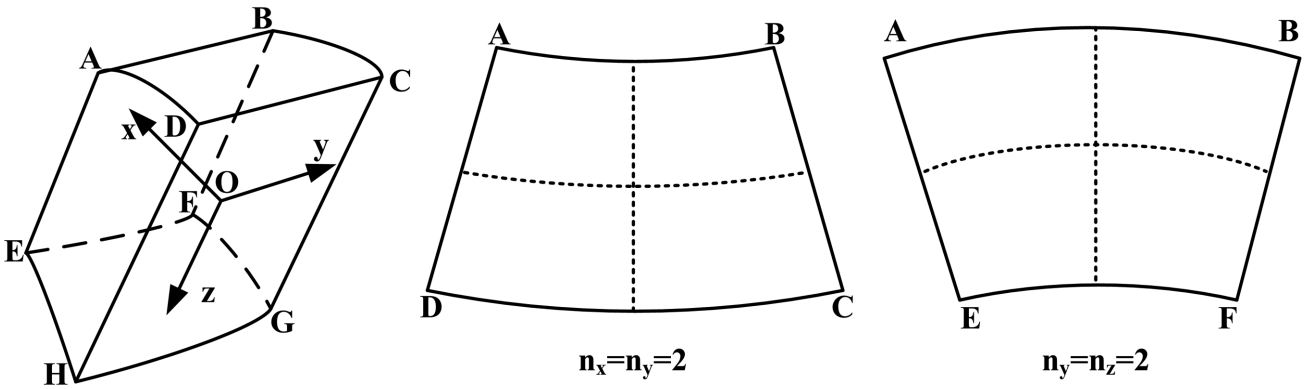

Figure 2. Sketch map of the subdivision of 2 × 2 × 2 for a spherical prism.

3 SUBDIVISION TECHNIQUE AND TRANSFORMATIONS BETWEEN DIFFERENT COORDINATE SYSTEMS

3.1 Subdivision technique

To obtain a more accurate result, we can subdivide the tesseroid into a number of tesseroids with small geometric scales (a subdivision of 2 × 2 × 2 for a SP is shown in Fig. 2). Assuming the numbers of subdivided tesseroids in latitude, longitude and radial are n_x, n_y and n_z, respectively, due to the principle of superposition, we can summarize the magnetic effects of each tesseroid to obtain the total magnetic effects as follows:

$$\begin{Bmatrix} V \\ B_i \\ B_{ij} \end{Bmatrix} = \sum_{m=1}^{n_x \times n_y \times n_z} \begin{Bmatrix} V(\mathbf{M}_m) \\ B_i(\mathbf{M}_m) \\ B_{ij}(\mathbf{M}_m) \end{Bmatrix}. \tag{39}$$

In this case, the direction of $\mathbf{M}_m$ in each subdivided tesseroid is constant in each subdivided tesseroid-centred Cartesian coordinates but variable in the whole tesseroid-centred Cartesian coordinates. Therefore, the subdivision technique can reduce the approximate error of the actually constant magnetized direction in the whole tesseroid-centred spherical coordinates. In general, the ratio among n_x, n_y and n_z can be determined by the geometric ratio of the 'equivalent' lengths in the three directions in eq. (38) approximately.

3.2 Coordinates and magnetic fields transformations

From the study above, there is the necessity to transform the magnetization vector, magnetic field vector and its gradient tensor from one local centred CCS to another local centred CCS. Here, supposing there are two local CCSs (**x**, **y**, **z**) and (**x***, **y***, **z***) shown in Fig. 3, where the origins are points $P(r, \varphi, \lambda)$ and $Q(r^*, \varphi^*, \lambda^*)$, respectively. With the aid of a conventional global geocentric CCS (**X**, **Y**, **Z**), we first give the position vector of point P in the point Q centred local CCS as:

$$\begin{bmatrix} x \\ y \\ z \end{bmatrix} = \mathbf{W} \begin{bmatrix} r\cos\varphi\cos\lambda - r^*\cos\varphi^*\cos\lambda^* \\ r\cos\varphi\sin\lambda - r^*\cos\varphi^*\sin\lambda^* \\ r\sin\varphi - r^*\sin\varphi^* \end{bmatrix}, \tag{40}$$

where the complete transformation matrix **W** is given by (Uieda 2012)

$$\mathbf{W} = \begin{bmatrix} -\sin(\varphi^*)\cos(\lambda^*) & -\sin(\varphi^*)\sin(\lambda^*) & \cos(\varphi^*) \\ -\sin(\lambda^*) & \cos(\lambda^*) & 0 \\ -\cos(\varphi^*)\cos(\lambda^*) & -\cos(\varphi^*)\sin(\lambda^*) & -\sin(\varphi^*) \end{bmatrix}. \tag{41}$$

Besides, the magnetic vector and gradient tensor in the spherical source point Q-centred local CCS are required to be expressed in the spherical observation point P-centred local CCS. According to the studies by Heck & Seitz (2007), Wild-Pfeiffer (2008) and Uieda (2012), these transformations can be performed as

$$\mathbf{B} = \mathbf{R}(\mathbf{B}^*), \tag{42}$$

$$\nabla\mathbf{B} = \mathbf{R}(\nabla\mathbf{B}^*)\mathbf{R}^{\mathrm{T}}, \tag{43}$$

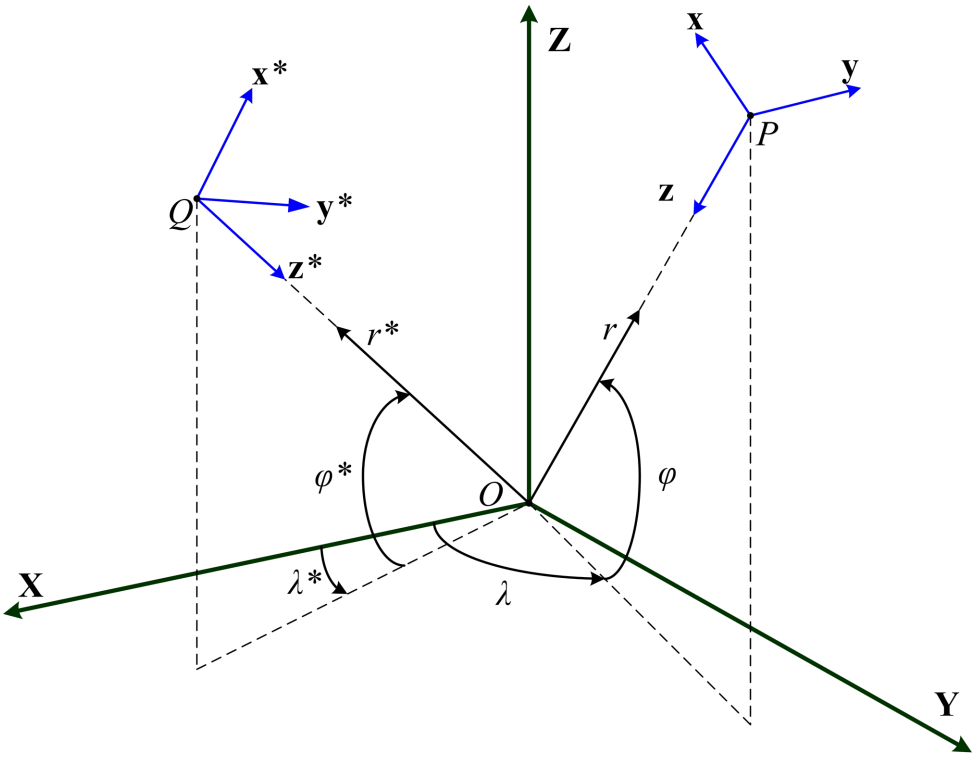

Figure 3. Sketch map of two spherical local CCSs (**x**, **y**, **z**) and (**x***, **y***, **z***) in the global geocentric SCS ($\mathbf{r}, \boldsymbol{\varphi}, \boldsymbol{\lambda}$) and the global geocentric CCS (**X**, **Y**, **Z**).

where the superscript $^{\mathrm{T}}$ stands for the transpose and corresponding transformation matrix is

$$\mathbf{R} = \begin{bmatrix} \cos\vartheta\sin\varphi\sin\varphi^* + \cos\varphi\cos\varphi^* & \sin\vartheta\sin\varphi & \cos\vartheta\sin\varphi\cos\varphi^* - \cos\varphi\sin\varphi^* \\ -\sin\vartheta\sin\varphi^* & \cos\vartheta & -\sin\vartheta\cos\varphi^* \\ \cos\vartheta\cos\varphi\sin\varphi^* - \sin\varphi\cos\varphi^* & \sin\vartheta\cos\varphi & \cos\vartheta\cos\varphi\cos\varphi^* + \sin\varphi\sin\varphi^* \end{bmatrix}, \tag{44}$$

and $\vartheta = \lambda^* - \lambda$. Likewise, the transformations for the magnetization vectors can be obtained as same as the procedure in eq. (42). Based on these transforms and the subdivision above, we can approximate both the actual variations of the magnetization's direction and also the geometric shape of the SP, so that the solutions with any required level of modelling accuracy will be obtained.

4 NUMERICAL INVESTIGATIONS

There are no theoretical values to directly evaluate the accuracy of all the methods. Therefore, first we compare the results at satellite altitude by our MD formulas and the RGLQI with those by previous method revised by Dyment & Arkani-Hamed (1998a) and GLQI by Asgharzadeh *et al.* (2008) to investigate the validity of our methods in Sections 2.4 and 2.5. Then with the aid of subdivided technique to obtain the approximated theoretical values, we evaluate the accuracies and computational efficiencies of all the forward methods without the subdivision with the computing points at different altitudes and the tesseroids at different locations, respectively. Finally, our 3-D RGLQI method is applied to calculate the magnetic effects based on a global lithospheric magnetization model.

4.1 Comparison with previous methods

A tesseroid with the geometric size of 0.25° × 0.25° × 30 km (i.e. about 28 km × 28 km × 30 km) and with the susceptibility of 0.05 SI, the magnetization declination and inclination of $D_Q = 45°$ and $I_Q = 45°$ and the strength of 50 000 nT for the inducing field is utilized here, which locates at equator and the upper surface of the tesseroid coincides with the Earth's magnetic reference sphere with radii of 6371.2 km (e.g. Finlay *et al.* 2010). We use the formulas (Dyment & Arkani-Hamed 1998a) of the MD to calculate the magnetic potential and vector at an altitude of 300 km in the region of 10°S–10°N and 10°W–10°E with data spaces of 0.125° and 0.125°. Then the magnetic potential and vector by the MD method in Section 2.5 is utilized to compare with those by previous method. The results by these two methods are completely same, which suggests the validity of the algorithms by Cartesian elements in Section 2.5 and further our MD method is extended to the magnetic gradient tensor fields. Besides, we also compare our revised GLQI method with that by Asgharzadeh *et al.* (2008) and the forward results by these two kinds of formulas are also completely same but our expressions are concise and thus the computational times

are decreased by our RGLQI method about 14 per cent for magnetic potential, 6 per cent for magnetic vector and 19 per cent for magnetic tensor, respectively.

4.2 Analysis of forward modelling error and computational efficiency

Adopting the same model as described in Section 4.1 but with the magnetized declination $D_Q = 0^\circ$ and the magnetized inclination $I_Q = 90^\circ$, we choose the magnetic potential V, B_z and B_{zz} components on behalf of all the magnetic effects above the geocentric axis of the tesseroid at the altitude of 300 km to investigate the convergences of all methods as the number of subdivision increasing. The results in Fig. 4 show that, as the number of subdivision increasing, the magnetic effects by all methods tend to the constant values, but the speeds of the convergences are different. The results in Fig. 4 show that the convergence rate of 3-D RGLQI with fist- and higher order node is the highest, which indicates that computational efficiencies of 3-D RGLQI with first- and higher order node are better than others. Based on the convergences in Fig. 4, the results by the 3-D RGLQI method with the subdividing numbers of 20 (in latitude) $\times$ 20 (in longitude) $\times$ 20 (in radial) in three directions and Gaussian nodes of 10 are utilized as the theoretical values. Using the approximated theoretical values, we investigate the relative errors of all methods without the subdivisions. The corresponding results of V, B_z and B_{zz} components along the latitudinal profiles with a constant longitude of 0° over the centre of the tesseroid are shown in Fig. 5, which suggest that the MD and 3-D RGLQI with zero-order node will lead to relatively large errors at the altitude of 300 km to higher than 0.01 per cent for magnetic potential and about 1 per cent for magnetic vector and gradient tensor. Besides, due to the difference of the calculation for the volume of each subdivided tesseroid, there is little difference between the results by MD and 3-D RGLQI with zero-order node, where the volume of former is accurate but the latter is approximated by integration. In addition, based on the Fig. 5, we find that the modelling accuracies of TSE are better than those by the MD and the 3-D RGLQI with zero-order node but a little worse than those by the RP and the 3-D RGLQI with first-order node. As same as the theoretical analysis in the Section 2.3, the error of V decays most slowly as l increasing but most quickly for B_{ij} for the TSE method. The errors of the magnetic potential by all methods are lower than those of the magnetic vector and gradient tensor and those of the gradient tensor is the highest, and all the maximum errors appear above and around the sources. In addition, there are some 'dips' in the Fig. 5. These 'dips' of the forward modelling errors are caused by the geometric differences between the tesseroid and its approximation by the dipole(s) or the RP. The similar 'dips' also exists in the forward modelling errors for gravity effects (e.g. Lane 2009; Li *et al.* 2011).

To analyse the forward modelling errors of all methods when the computing points are at a low altitude, the same model as described above in Section 4.2 but with the altitude of 30 km for the observations is adopted here. Similarly with Fig. 4, the Fig. 6 shows the convergences of all methods as the number of subdivision increasing but the speeds of the convergences become slower than those in Fig. 4. According to the convergences in Fig. 6, the forward modelling results by the 3-D RGLQI method with the subdividing numbers of 20 (in latitude) $\times$ 20 (in longitude) $\times$ 20 (in radial) in three directions and Gaussian nodes of 10 are still utilized as the theoretical values. The profiles of the relative errors in Fig. 7 show that all the errors at the altitude of 30 km are higher than those at the altitude of 300 km and the theoretical values are also increased at the same time. As the Gaussian nodes increasing, the modelling accuracies of RGLQI become better and better but are improved very slowly near the sources. Modelling by the RP also shows the relatively accurate results but becomes worse when the tesseroid get close to the Earth's pole (Fig. 8, where the tesseroid is located at 86°N and 0°E). In fact, all the methods are influenced by the shape of the source but the RP is the worst. This indicates that the RP method is relatively worse to be utilized when the source located at the high latitude. However, the geometric shape of the tesseroid almost has relatively little impacts on the modelling errors by TSE and 3-D RGLQI. Because of the volume of the source is decreased when the tesseroid get close to the Earth's pole, there is a better accuracy. Both Figs 7 and 8 show that the modelling errors will be deduced when the computing points far away the source. Thus to understand the speed of error's decay with distance increasing, we use the same model located at the equator to calculate the relative errors by all methods as the altitudes of computing points increasing. The corresponding results in Fig. 9 depict that (i) the errors of 3-D RGLQI with the Gaussian node of higher than second-order decay very quickly and (ii) there are the differences between the errors by odd-order and even-order 3-D GLQI methods because of the different distribution of Gaussian nodes (e.g. Wild-Pfeiffer 2008). The errors of the TSE being similar with first-order 3-D RGLQI decay more quickly than those of the MD method and the zero-order GLQI method. Besides, the errors of the RP method is lower than those by the first-order 3-D RGLQI at the low altitude and tend to be constant from a higher altitude.

To investigate the computational efficiency, we first obtained the relative time of all methods using the same model and the same number of subdivision (n_x, n_y and n_z). As the number (M, N, L) of the Gaussian nodes increasing, the error by the 3-D RGLQI decreases, however, at the same time, the computing time rises at a high rate nearly proportional to $(M+1)^{n_x}(N+1)^{n_y}(L+1)^{n_z}$ (shown in Table 1 and Fig. 10). Nevertheless, the subdivision technique can be used to improve the accuracy and reduce the computational burden of each method in an actual application. If the maximum relative error is given to be 0.01 per cent at the altitude of 30 km, we statistically analyse the required subdivision numbers and relative computing times of all methods shown in Table 2. The results show that (i) the computing time of the magnetic potential is generally lower than those of the magnetic vector and the gradient tensor and (ii) the required number of subdivision is reduced as the order of Gaussian node increasing but the corresponding computational time is not always decreased, which indicates that choosing a reasonable numbers of the Gaussian node and the subdivision will produce the highest efficiency. In this example, the reasonable numbers of Gaussian node and subdivision should be in the range of 3–4 and 1–2, respectively.

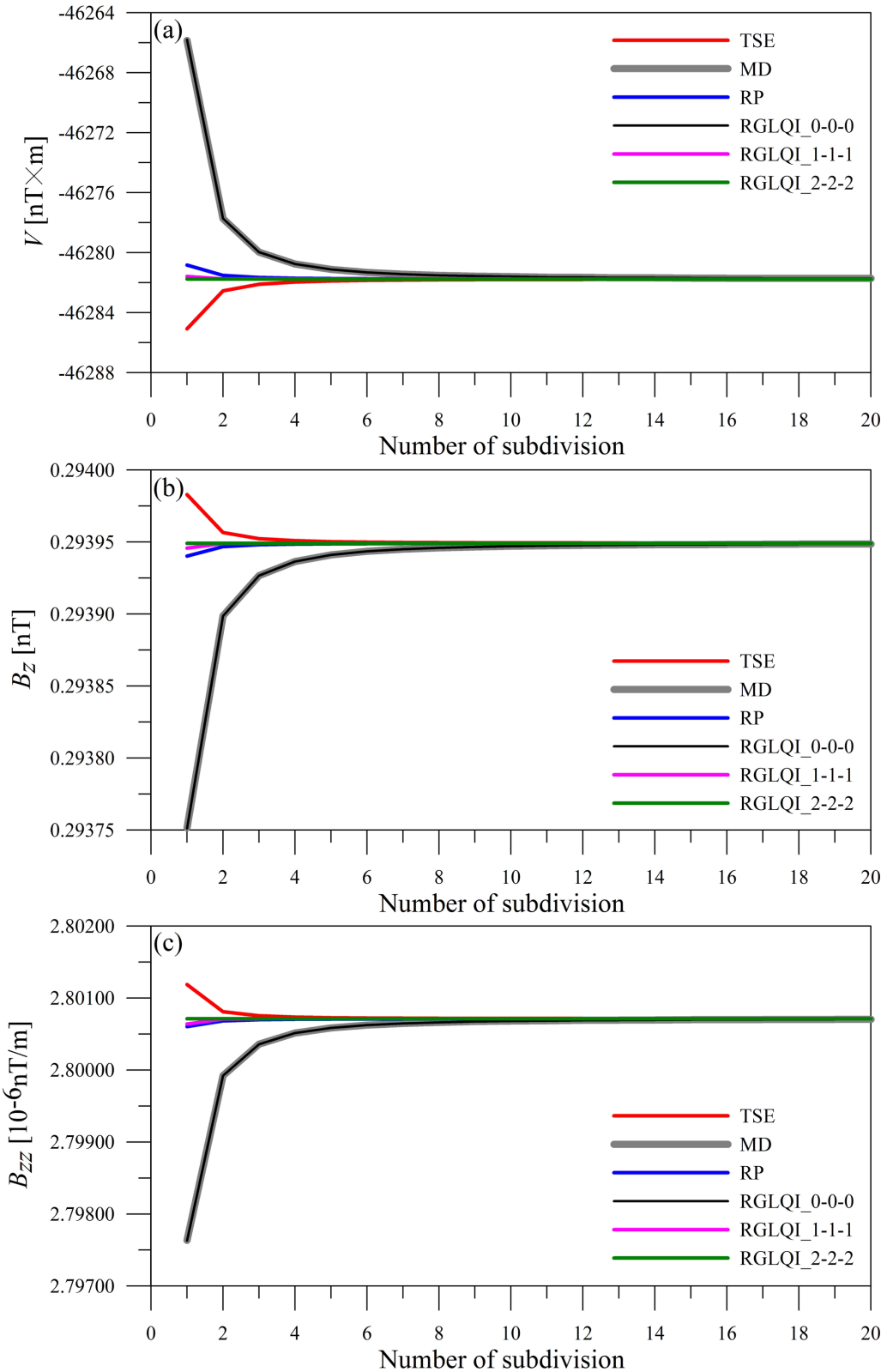

Figure 4. Convergence of forward modelling V, B_z and B_{zz} components by the different method as the numbers of subdivisions increasing along the latitudinal profiles with constant longitude of 0° over the centre of the tesseroid. Magnetic fields caused by a tesseroid at an altitude at 300.0 km relative to the Earth's magnetic reference sphere (i.e. 6371.2 km). The tesseroid with the size of 0.25° × 0.25° × 30 km and with the susceptibility of 0.05 SI, the magnetization declination and inclination of $D_Q = 0°$ and $I_Q = 90°$ and the strength of 50 000 nT for the inducing field is utilized. The tesseroid is located at (0°, 0°).

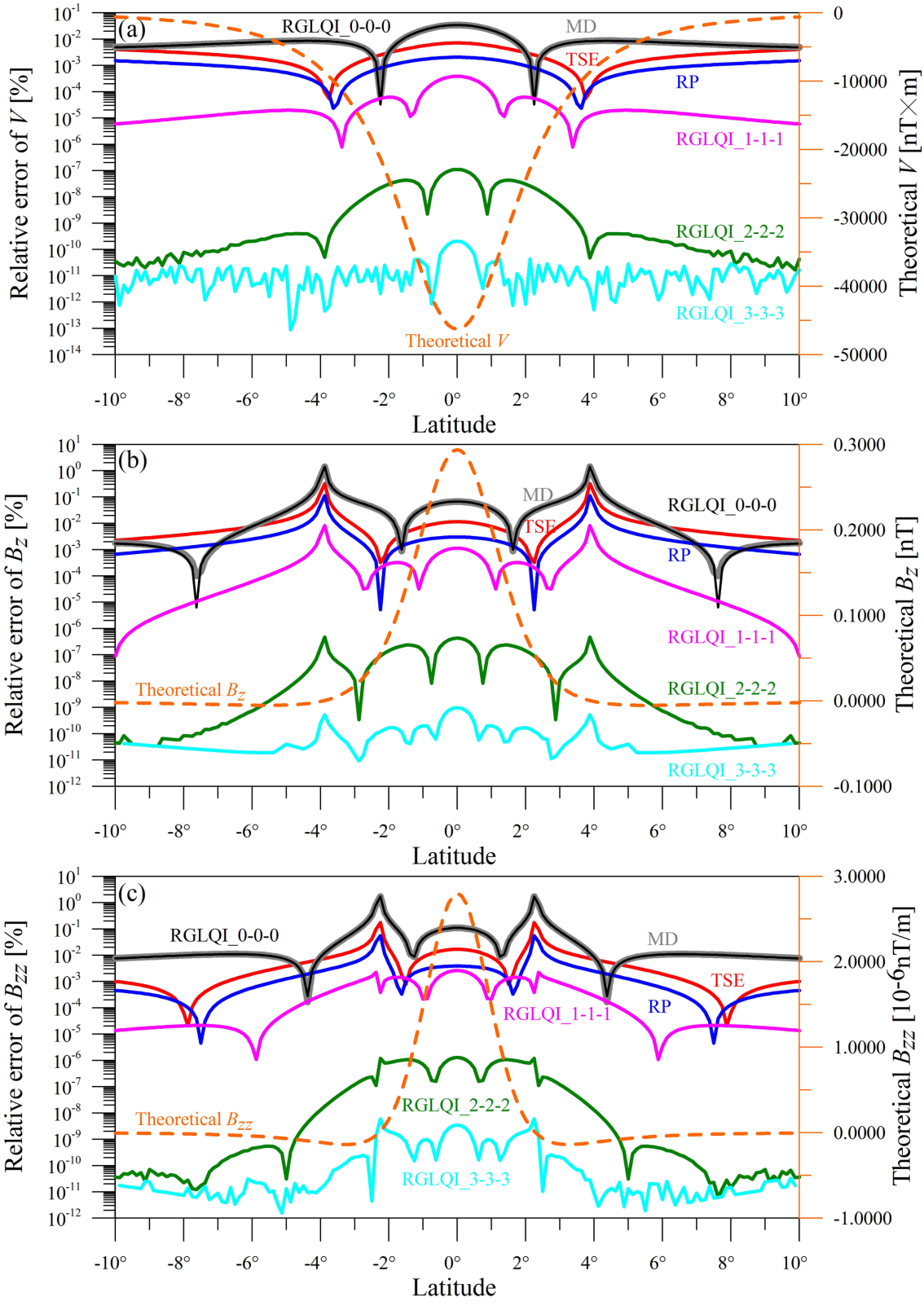

Figure 5. Profiles of the relative percentage errors in the form of a log-plot for the magnetic potential V, vector component B_z and tensor element B_{zz} at the altitude of 300 km along the longitude of 0° by different forward modelling method. The parameters of the model are same as those in Fig. 4.

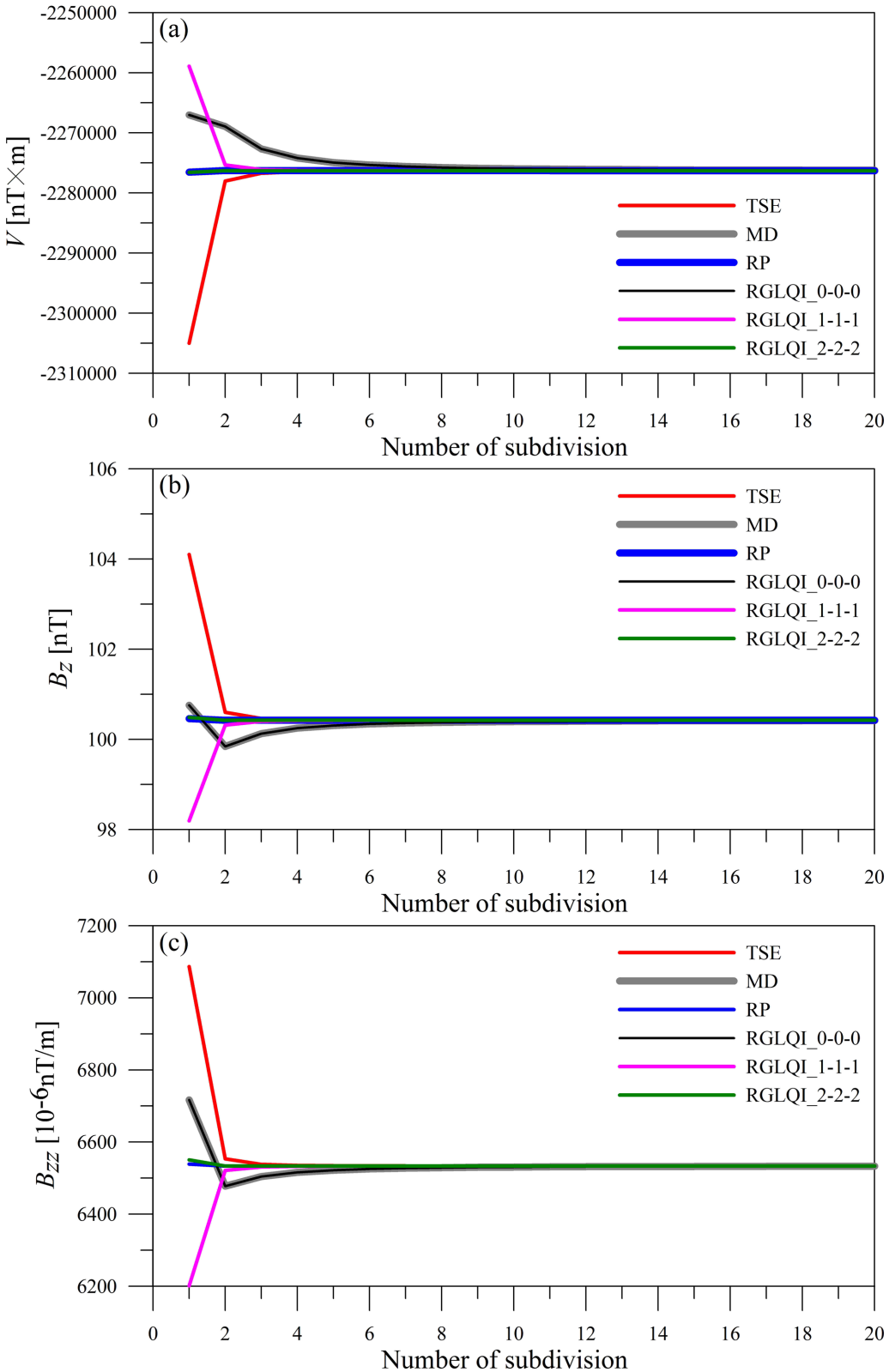

Figure 6. Convergence of forward modelling V, B_z and B_{zz} components at the altitude of 30 km by the different method as the numbers of subdivisions increasing along the latitudinal profiles with constant longitude of 0° over the centre of the tesseroid. The parameters of the model are same as those in Fig. 4.

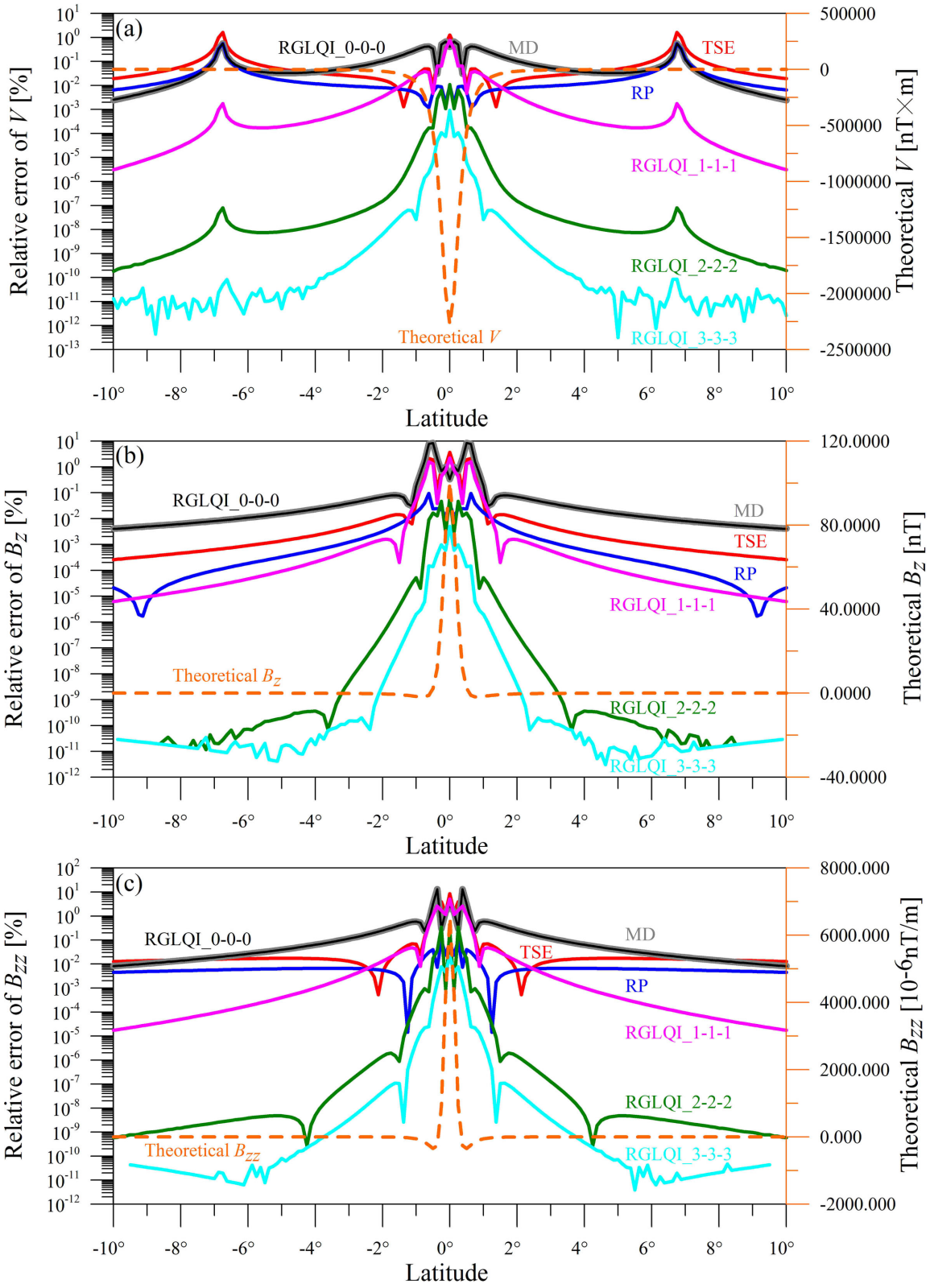

Figure 7. Profiles of the relative percentage errors in the form of a log-plot for the magnetic potential V, vector component B_z and tensor element B_{zz} at the altitude of 30 km along the longitude of 0° by different forward modelling method. The parameters of the model are same as those in Fig. 6.

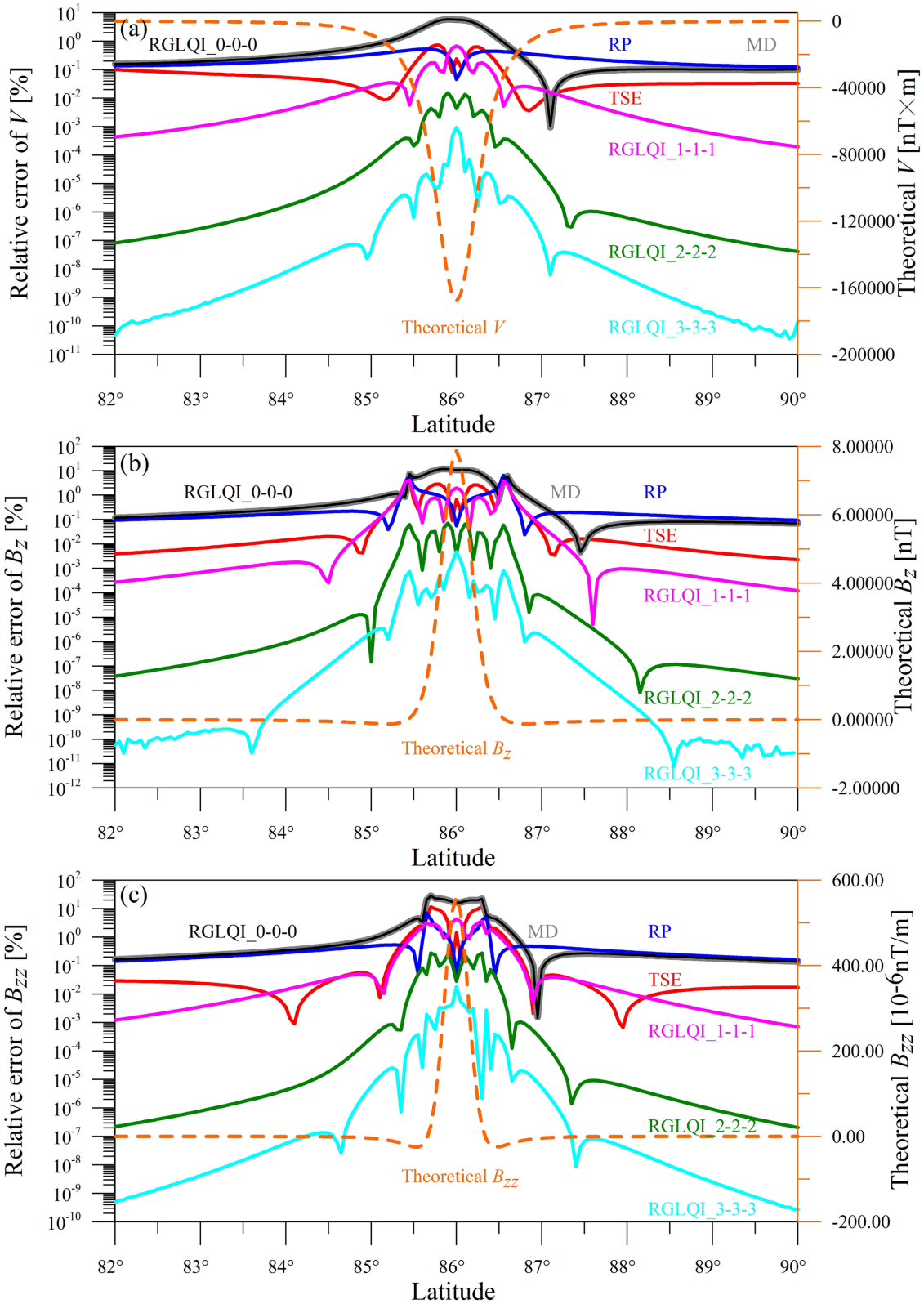

Figure 8. Profiles of the relative percentage errors in the form of a log-plot for the magnetic potential V, vector component B_z and tensor element B_{zz} at the altitude of 30 km along the longitude of 0° by different forward modelling method. The parameters of the model are same as those in Fig. 6 but the tesseroid is located at (89.6°N, 0°).

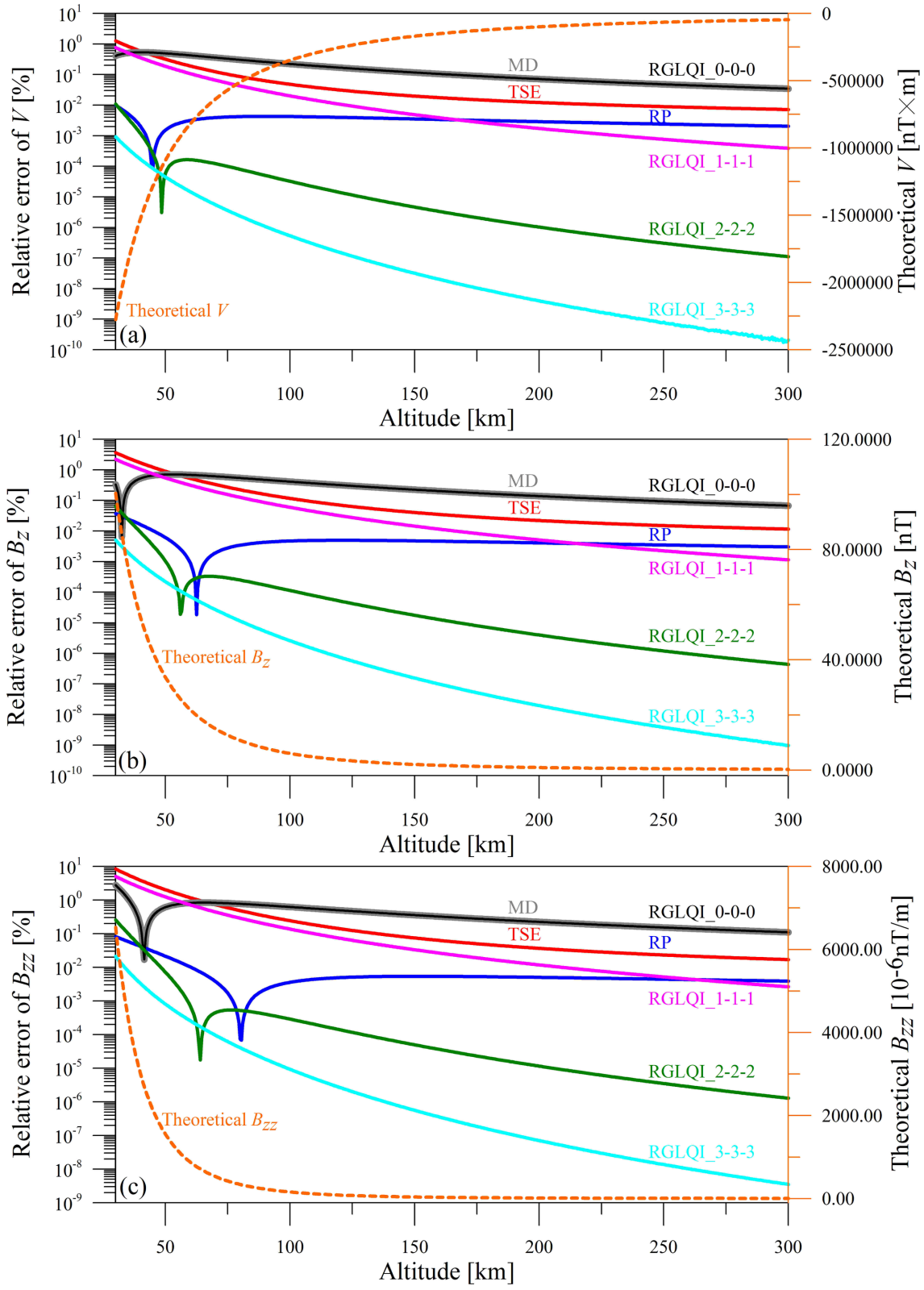

Figure 9. Relative percentage errors in the form of a log-plot changing with altitudes of computing points for the magnetic potential V, vector component B_z and tensor element B_{zz} by different forward modelling methods. The parameters of the model are same as those in Fig. 7. The computing points are just above the centre of the tesseroid. Data space is 0.5 km in altitude direction.

Table 1. Relative computational times for different forward modelling methods without any subdivision.

Method	Relative time of V	Relative time of B_z	Relative time of B_{zz}
MD	69.2	86.5	103.8
RP	207.6	259.5	173.0
TSE	86.6	103.8	138.4
RGLQI_0-0-0	34.6	34.6	51.9
RGLQI_1-1-1	224.9	294.1	311.4
RGLQI_2-2-2	761.2	1003.5	1003.5
RGLQI_3-3-3	1851.2	2370.2	2370.2
RGLQI_4-4-4	3529.4	4636.7	4654.0
RGLQI_5-5-5	6003.5	7906.6	8114.2
GLQI_5-5-5	6989.6	8373.7	10 000.0*

MD, magnetic dipole; RP, rectangular prism; TSE, Taylor's series expansion; RGLQI_0-0-0, revised Gauss–Legendre quadrature integration with Gaussian node of zero; GLQI_5-5-5, Gauss–Legendre quadrature integration with Gaussian node of five. *The time corresponding to 10 000.0 is utilized as the maximum to calculate the relative times for all the magnetic effects.

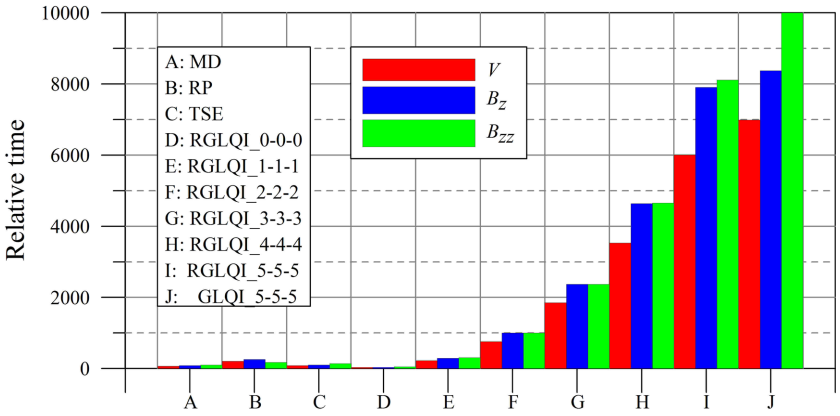

Figure 10. Relative computational times for different forward modelling methods without any subdivision. The parameters are the same as those of the model in Fig. 7.

4.3 Application to a global lithospheric magnetization model

To demonstrate the actual application of the 3-D RGLQI method, the magnetic potential, vector and gradient tensor fields at 300 and 30 km altitudes above the Earth's magnetic reference sphere, respectively, are computed globally using a global lithospheric magnetization model. Meanwhile, the results by the traditional MD method based on the same magnetization model are calculated and compared with those by the 3-D RGLQI method.

The global lithospheric magnetization model with a resolution $0.25^\circ \times 0.25^\circ$ is constructed by combing the oceanic remanent magnetization model of Masterton *et al.* (2013) and the induced magnetization model of Hemant & Maus (2005). This VIM model is multiplied by

Table 2. Required numbers of subdivisions and the corresponding relative computational times for different forward modelling methods providing the maximum error is lower than 0.01 per cent.

Method	Required number of subdivision			Relative time		
	V	B_z	B_{zz}	V	B_z	B_{zz}
MD	13 × 13 × 13	26 × 26 × 26	32 × 32 × 32	1388.9	3777.8	10 000*
RP	8 × 8 × 8	3 × 3 × 3	3 × 3 × 3	85.5	2.7	1.7
TSE	13 × 13 × 13	5 × 5 × 5	6 × 6 × 6	85.5	7.5	16.8
RGLQI_0-0-0	13 × 13 × 13	26 × 26 × 26	32 × 32 × 32	79.4	1555.6	4000
RGLQI_1-1-1	3 × 3 × 3	4 × 4 × 4	5 × 5 × 5	2.9	9.3	25.2
RGLQI_2-2-2	2 × 2 × 2	2 × 2 × 2	2 × 2 × 2	2.7	2.9	2.9
RGLQI_3-3-3	1 × 1 × 1	1 × 1 × 1	2 × 2 × 2	0.6	0.8	6.7
RGLQI_4-4-4	1 × 1 × 1	1 × 1 × 1	1 × 1 × 1	1.2	1.5	1.5
RGLQI_5-5-5	1 × 1 × 1	1 × 1 × 1	1 × 1 × 1	2.2	2.6	2.6
GLQI_5-5-5	1 × 1 × 1	1 × 1 × 1	1 × 1 × 1	2.6	2.8	3.2

*The time corresponding to 10 000.0 is utilized as the maximum to calculate the relative times for all the magnetic effects providing the maximum error is lower than 0.01 per cent. Note here that the reference value 10 000 in Table 2 is different from the reference value 10 000 in Table 1.

an averaged thickness of global magnetized lithosphere to derive a global ellipsoidal single layer model. In this paper, the average thickness of 26.5 km (Vervelidou & Thébault 2014) and the WGS84 reference ellipsoid as the top surface of the VIM are adopted.

According to the analysis in Section 4.2, the necessary numbers of the Gaussian nodes and subdivisions are determined to be $1\times1\times1$ and $1 \times 1 \times 1$ at the altitude of 300 km and $4 \times 4 \times 4$ and $1 \times 1 \times 1$ at the altitude of 30 km, respectively. However, for every computing point, because of the horizontal decay of the magnetic effects, there may be no necessity to calculate the global contributions. Fig. 11 demonstrates the decay features of the V, B_x, B_z and B_{xx}, B_{zx}, B_{zz} components (representatives for all the magnetic effects), where the inclination and the declination of the inducing field are 0° and 0° since in this case the horizontal decay is slowest than those with other inclinations. The profiles of amplitude normalized curves are along the longitude of 0° from the central axis of the SP at the equator. The results in Fig. 11 show that the magnetic potential V decays more slowly than those of other components, and the decay at the altitude of 30 km is more quickly than that at the altitude of 300 km. Based on these decay features, to improve the computational efficiency but not affect the accuracy too much, as expected, only the magnetic sources inside the spherical angles of 35° at the altitude of 300 km and 5° at the altitude of 30 km are roughly taken into the computation. Adopting the MD method, in this case, the accuracy is expected to be ensured because of the long distance between the sources and the computing point. The magnetic effects by the magnetic sources beyond the spherical angles of 35° at the altitude of 300 km and 5° at the altitude of 30 km are shown in Figs 12 and 13, respectively, which are dominated by the long wavelength components but the amplitudes are not very low. Furthermore, because of the different decay features, the effect of the magnetic potential is the strongest and that of the gradient is the weakest. Therefore, if modelling the relatively long wavelengths field (e.g. Meyer *et al.* 1985) or 3-D inversion (Du *et al.* 2014), these magnetic effects from outside should be reasonably considered.

Utilizing the forward parameters above, the magnetic effects of the global VIM at the altitudes of 300 and 30 km are calculated and shown in Figs 14 and 15, respectively. The results in Figs 14 and 15 suggest that, (i) the magnetic potential, vector and gradient tensor are in the range of about -1.242×10^7–$+1.148 \times 10^7$ nT·m, −31.549–+36.743 nT and −0.162–+0.187 pT m^{-1} at the altitude of 300 km and

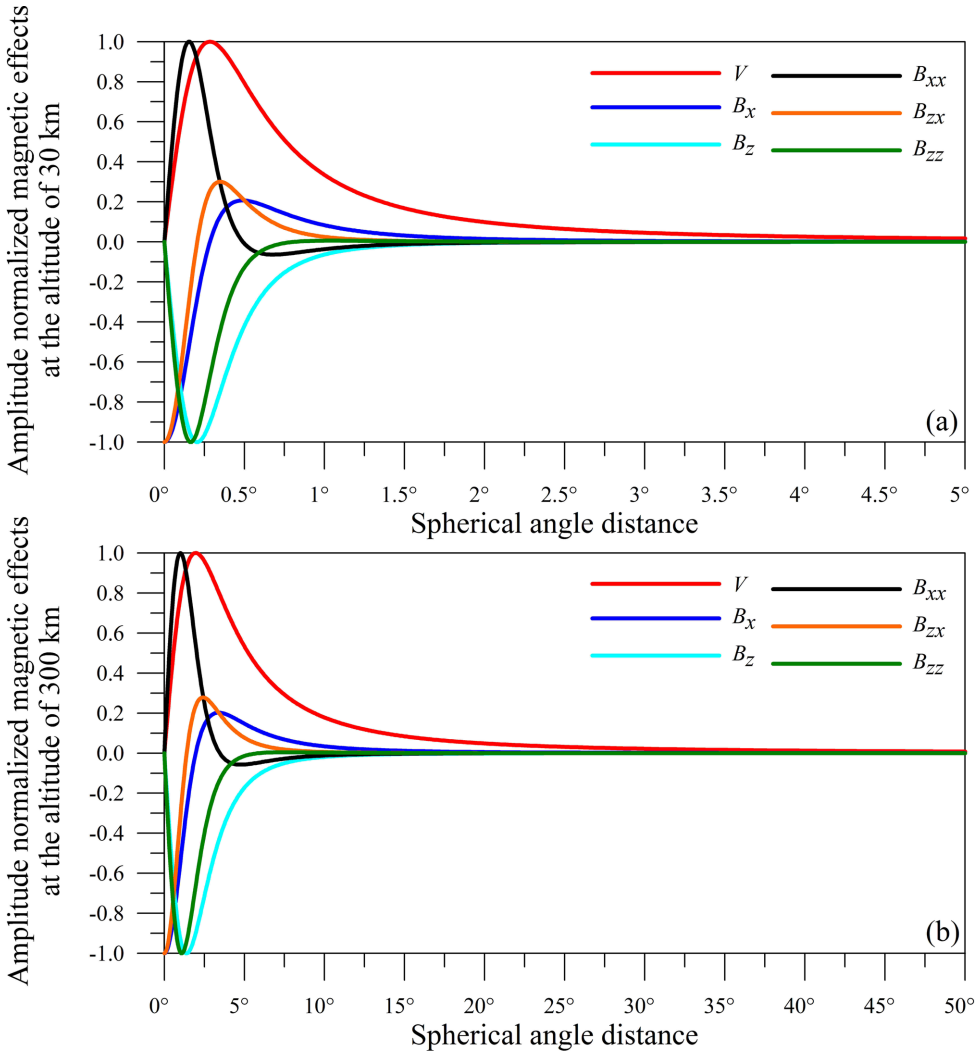

Figure 11. The horizontal decay features of the V, B_x, B_z and B_{xx}, B_{zx}, B_{zz} components at the altitudes of 30 km (a) and 300 km (b), where the inclination and the declination of the inducing field are 0° and 0°. The profiles of amplitude normalized curves are along the longitude of 0° from the central axis of the spherical prism. The other parameters are the same as those in Figs 7 and 8.

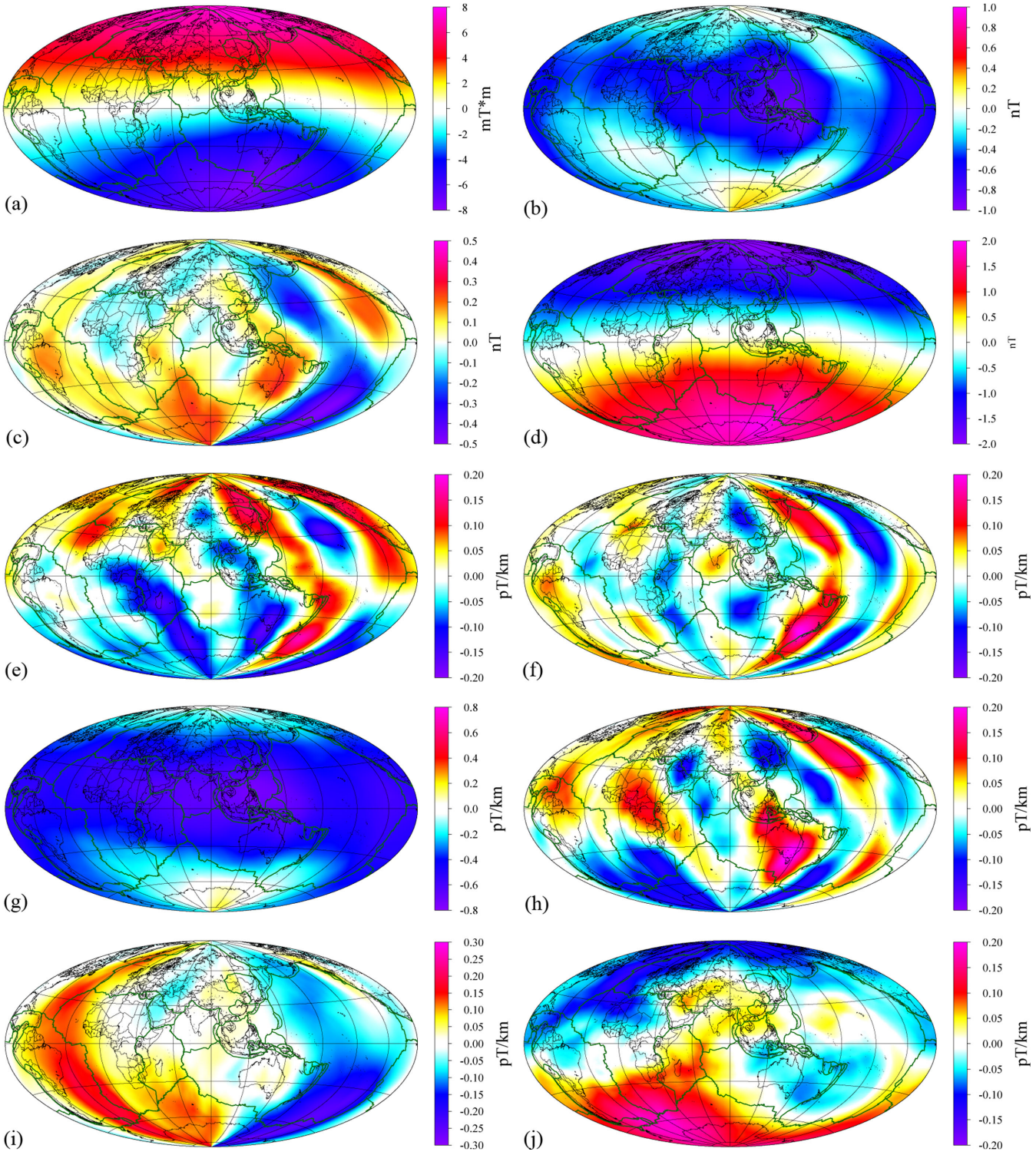

Figure 12. The magnetic effects of the VIM beyond the spherical angles of 35° at the altitudes of 300 km by the MD method. (a) is the magnetic potential V, (b), (c) and (d) are the B_x, B_y and B_z components of the magnetic vector and (e)–(j) are the B_{xx}, B_{xy}, B_{xz}, B_{yy}, B_{yz} and B_{zz} elements of the magnetic gradient tensor. The dark green lines are the plate boundaries by Bird (2003). All maps are shown on a Hammer projection centred at 90°E.

about -3.659×10^7–$+3.684 \times 10^7$ nT·m, -427.309–$+352.048$ nT and -11.020–$+10.800$ pT m^{-1} at the altitude of 30 km and (ii) the values of $B_{xx} + B_{yy} + B_{zz}$ are almost equal to be zeros if ignoring the computing round-off errors which indirectly indicates the validity of our methods. Meanwhile, we also employ the MD method to compute the magnetic effects by the global VIM. The differences between the magnetic effects by the 3-D RGLQI and the MD method at the altitude of 300 km are very weak. As illustrated in Fig. 16, at the altitude of 30 km these differences are very strong relative to the results at the altitude of 300 km, especially in the low/middle latitudes. The relative errors of the magnetic potential, vector and gradient tensor are about 0.25 per cent, 1 per cent and 10 per cent, respectively. These levels of the

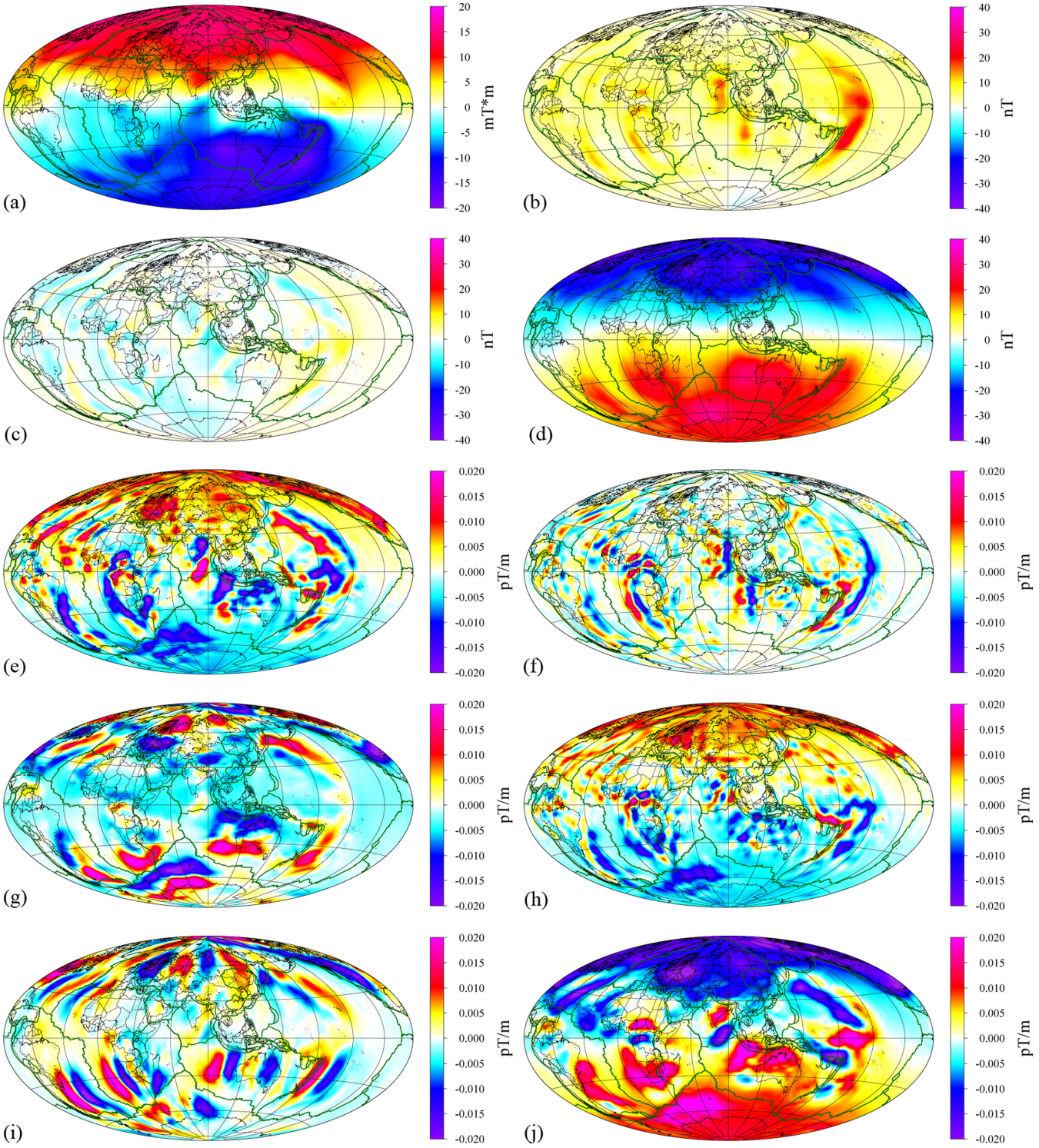

Figure 13. The magnetic effects of the VIM beyond the spherical angles of 5° at the altitudes of 30 km by the MD method. (a) is the magnetic potential V, (b), (c) and (d) are the B_x, B_y and B_z components of the magnetic vector and (e)–(j) are the B_{xx}, B_{xy}, B_{xz}, B_{yy}, B_{yz} and B_{zz} elements of the magnetic gradient tensor. The dark green lines are the plate boundaries by Bird (2003). All maps are shown on a Hammer projection centred at 90°E.

relative errors coincide with the results in Fig. 9. The relative errors of the magnetic potential and vector are lower than that of the gradient tensor, which is caused by the 'dips' in Fig. 9. If the tesseroids with larger geometric size but not the size of $0.25^\circ \times 0.25^\circ$ are used here, the relative errors in Figs 9 and 16 will increase. Therefore, the error analysis suggests that the MD method is more valid at the high altitude of the computing point and will introduce relatively large errors when the computing points at the low altitudes.

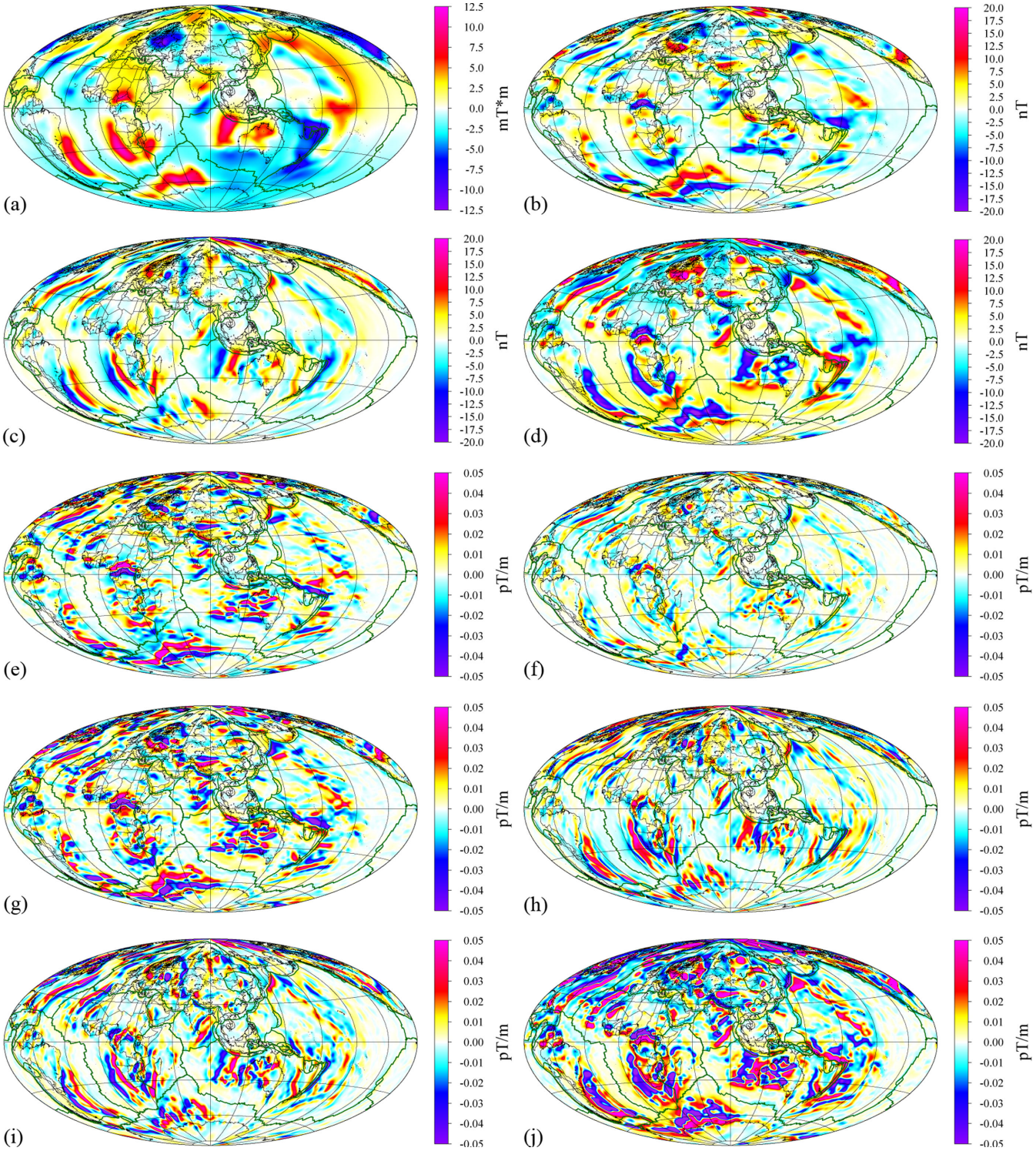

Figure 14. The magnetic effects of the global VIM at the altitudes of 300 km by the 3-D RGLQI with 1 × 1 × 1 as the number of Gausian nodes and 1 × 1 × 1 as the number of subdivision. (a) is the magnetic potential V, (b), (c) and (d) are the B_x, B_y and B_z components of the magnetic vector and (e)–(j) are the B_{xx}, B_{xy}, B_{xz}, B_{yy}, B_{yz} and B_{zz} elements of the magnetic gradient tensor. The dark green lines are the plate boundaries by Bird (2003). All maps are shown on a Hammer projection centred at 90°E.

5 DISCUSSION AND CONCLUSIONS

As the simple and popular volume discretization in geodetic or geocentric spherical coordinate system (SCS), the tesseroid directly incorporate the curvature of the Earth and thus is chosen naturally to process and interpret the regional and global magnetic anomaly field data. However, the magnetic effects of the tesseroid comprise elliptical integrals that cannot be solved analytically. Referring to the forward methods for

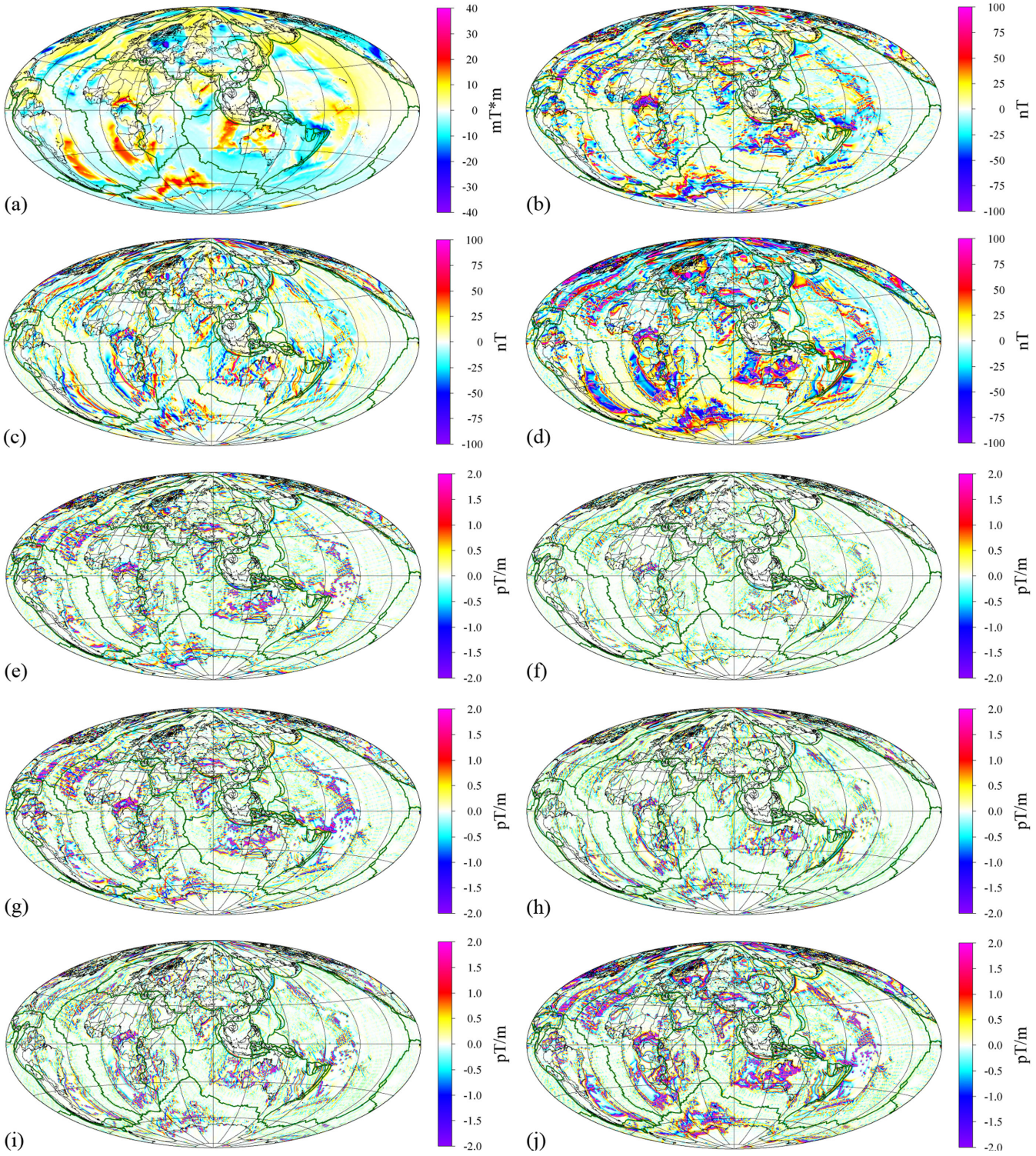

Figure 15. The magnetic effects of the global VIM at the altitudes of 30 km by the 3-D RGLQI with 4 × 4 × 4 as the number of Gausian nodes and 1 × 1 × 1 as the number of subdivision. (a) is the magnetic potential V, (b), (c) and (d) are the B_x, B_y and B_z components of the magnetic vector and (e)–(j) are the B_{xx}, B_{xy}, B_{xz}, B_{yy}, B_{yz} and B_{zz} elements of the magnetic gradient tensor. The dark green lines are the plate boundaries by Bird (2003). All maps are shown on a Hammer projection centred at 90° E.

gravity effects in the literature, we systematically present three kinds of forward modelling methods for the magnetic effects of the tesseroid in the geocentric SCS, including the TSE method, the revised GLQI approach and the approximations by traditional Cartesian elements, such as the MD and RP. The nature of our formulas is same with that by Asgharzadeh *et al.* (2008), but based on the Cartesian integral kernels (Grombein *et al.* 2013) and the assumption that the magnetized direction is constant our derived formulas are simpler and thus the computing time is reduced. The MD method is also naturally same with that by Dyment & Arkani-Hamed (1998a), but based on the general frame by

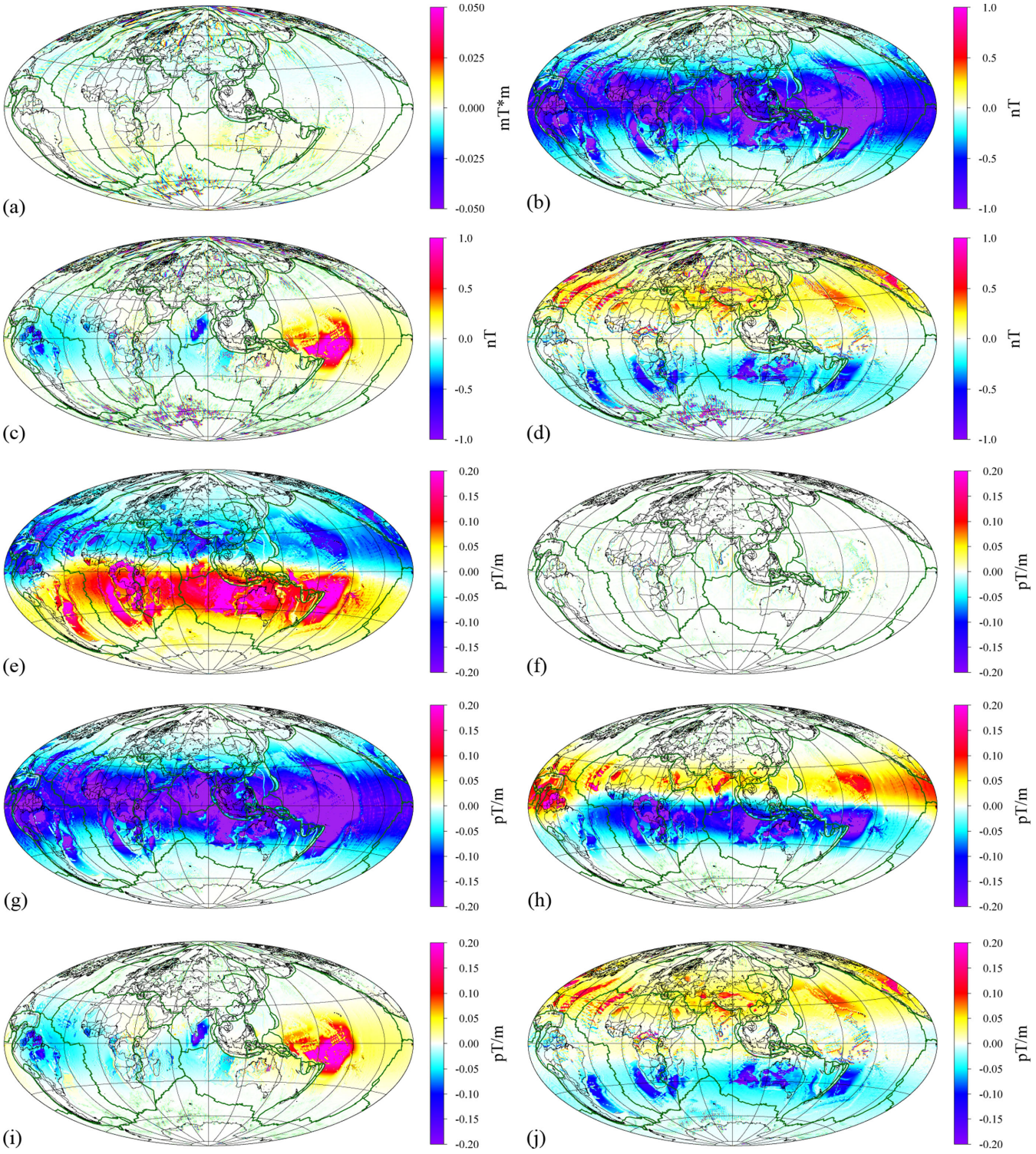

Figure 16. The differences between the magnetic effects of the global VIM at the altitudes of 30 km by the 3-D RGLQI and those by the MD method. (a) is the magnetic potential V, (b), (c) and (d) are the B_x, B_y and B_z components of the magnetic vector and (e)–(j) are the B_{xx}, B_{xy}, B_{xz}, B_{yy}, B_{yz} and B_{zz} elements of the magnetic gradient tensor. The dark green lines are the plate boundaries by Bird (2003). All maps are shown on a Hammer projection centred at 90° E.

the Cartesian elements, we extend the MD method to forward modelling the magnetic gradients and other elements such as lines and layers can be easily utilized. Besides, the magnetic effects caused by a 2-D geological source can also be obtained through this frame. However, it is difficult to balance the computing accuracy and the time if any single forward modelling method is employed. Therefore, we utilize the subdivision technique, which makes it available to forward model the magnetic potential, vector and gradient tensor fields at any position on the globe caused by the tesseroid with any geometric scale.

By numerical tests, we compared the computing accuracy of the forward modelling methods and some conclusions are summarized as follows:

(i) The accuracy of the presented approaches is mainly sensitive to the distance between the source point and the computation point and also the tesseroid's geometrical shape and size changing with the latitude and depth of the source.

(ii) The accuracy of the magnetic potential is higher than that of the vector or tensor response. The tensor errors are the largest but they decrease more quickly with distance from the source.

(iii) Since the geometrical differences of the dipole, a set of the dipoles and the RP with the tesseroid, there are some 'dips' in the forward modelling errors. The locations of these 'dips' are mainly dependant on the geometrical shape of the source.

(iv) The GLQI with zero-order node has an almost same accuracy with that of the MD method. The difference between them just is the calculation for the volume of the prism. The volume for the MD is accurate but for the GLQI is approximated by integration.

(v) The accuracy of TSE is better than that by the MD or the 3-D RGLQI with zero-order node but a little worse than those by the 3-D RGLQI with first- and higher-order nodes.

(vi) If the source located in a low latitude region, the modelling accuracy by RP is relative better than those of the MD, TSE and the 3-D RGLQI with zero- and first-order nodes in the near zone but becomes more and more worse when the source towards the polar regions.

(vii) The numbers of the Gaussian node in the radial, latitude and longitude directions are better to be determined by the geometrical ratio of the 'equivalent volume' RP. As the number of the Gaussian node increases, the accuracy of the 3-D GLQI becomes better and better. However, at the short distance from the source, the rate of convergence is very slow.

(viii) Due to the subdivision technique, the accuracies of all methods are improved but the rates of convergence are different, where the RP and the 3-D GLQI with second- and higher-order nodes have the fastest convergence speed as the number of the subdivision increasing.

We also numerically investigate the computing efficiency of the forward modelling methods and some points come in mind below:

(i) Purely considering the computing time for all methods without any subdivision, in general, the magnetic potential is fastest and the gradient tensor is slowest. The computing times of the 3-D GLQI with zero-order node, the MD, the TSE, the RP and the 3-D GLQI with first- and higher order nodes successively increase. As the number (M, N, L) of the Gaussian nodes increasing, the computing time rises at a high rate nearly proportional to $(M+1)(N+1)(L+1)$. If the number (n_x, n_y, n_z) of the subdivision is used, the computing time of the 3-D GLQI rises at a high rate nearly proportional to $(M+1)^{n_x}(N+1)^{n_y}(L+1)^{n_z}$.

(ii) Providing the maximum error is given, the required number of the subdivision and the corresponding computing time of each method are different. The MD and the 3-D GLQI with zero-order node are the most time-consuming. As the number of the Gaussian node increasing, the required number of the subdivision reduces but the corresponding computing time is not always decrease. There is the most optimal number of Gaussian node but will vary if the source and location of the observation changing. Combined with the suitable number of subdivisions, the GLQI method with reasonable number of Gaussian nodes is the best forward modelling method. Therefore, in the actual applications, the optimal numbers of the subdivision and Gaussian node should be investigated in advance.

In the actual applications using the tesseroids with the geometrical size of $0.25^\circ \times 0.25^\circ$, we obtain some conclusions as follows:

(i) At the satellite altitude such as 300 km, the relative errors of the magnetic potential, vector and gradient tensor by the MD method are lower than 0.1, 2 and 2 per cent, respectively. However, at the low altitude such as 30 km, the relative errors of the magnetic potential, vector and gradient tensor by the MD method are higher than 1, 10 and 10 per cent, respectively.

(ii) For one tesseroid, the magnetic effects will decay to a very low value close to zero as the distance from the source increasing. Therefore, in traditional, only the contributions of the sources inside a special region are considered. However, our results show that the contributions of the sources out the region are not very low and dominated by long wavelengths, which should not be ignored.

The derived formulas and their calculating algorithms in this paper will sever the purpose that the 3-D magnetization structure modelling with lithospheric vertical scales and global, continent or large regional horizontal scales (Du *et al.* 2013, 2014). Meanwhile, this work is also helpful into magnetic field modelling, data processing and interpretations by inversing approaches (e.g. Whaler 1994; Purucker *et al.* 2002; Kim *et al.* 2013). Nevertheless, in this paper, the numbers of Gaussian nodes and the subdivisions are uniform, which results into much price to pay for the computing time. Therefore, in the near future, based on the error attenuation feature of the magnetic effects, an adaptive frame will be developed according to the distance between the source point and the computation point, for example the approach performed by Dransfield (1994), Li *et al.* (2011) and Uieda *et al.* (2011) for gravity effects.

ACKNOWLEDGEMENTS

This study has been supported by the International Cooperation Projection in Science and Technology (Grant No.: 2010DFA24580). Jinsong Du is sponsored by the China Scholarship Council and the computation server is provided by the Section 2.3 in German Research Center for Geosciences (GFZ). This work is also supported in part through a collaborative research project bringing together the China University of Geosciences, Colorado School of Mines and Geoscience Australia. All projected figures are drawn using The Generic Mapping Tools (GMT; Wessel & Smith 1991).

REFERENCES

An, Y.L. & Guan, Z.N., 1990. Direct and inverse methods of magnetic anomaly engendered by magnetic layer with spherical shell shape, *Geosci., J. Grad. School* (in Chinese), **4**(2), 116–129.

Anderson, E.G., 1976. *The effect of topography on solutions of Stokes' problem,* Unisurv. S-14, Rep., School of Surveying, University of New South Wales, Kensington.

Arkani-Hamed, J. & Strangway, D.W., 1985. Lateral variation of apparent magnetic susceptibility of lithosphere deduced from Magsat data, *J. geophys. Res.,* **90,** 2655–2664.

Asgharzadeh, M.F., von Frese, R.R.B., Kim, H.R., Leftwich, T.E. & Kim, J.W., 2007. Spherical prism gravity effects by Gauss-Legendre quadrature integration, *Geophys. J. Int.,* **169,** 1–11.

Asgharzadeh, M.F., von Frese, R.R.B. & Kim, H.R., 2008. Spherical prism magnetic effects by Gauss-Legendre quadrature integretion, *Geophys. J. Int.,* **173,** 315–333.

Barnett, C.T., 1976. Theoretical modeling of the magnetic and gravitational fields of an arbitrarily shaped three-dimensional body, *Geophysics,* **41,** 1353–1364.

Bhattacharyya, B.K., 1964. Magnetic anomalies due to prism-shaped bodies with arbitrary polarization, *Geophysics,* **XXIX**(4), 517–531.

Bhattacharyya, B.K., 1966. Continuous spectrum of the total-magnetic field anomaly due to a rectangular prismatic body, *Geophysics,* **31,** 97–121.

Bird, P., 2003. An updated digital model of plate boundaries, *Geochem. Geophys. Geosyst.,* **4**(3), 1027, doi:10.1029/2001GC000252.

Blakely, R.J., 1995. *Potential Theory in Gravity & Magnetic Applications,* Cambridge Univ. Press.

Bott, M.H.P., 1963. Two methods applicable to computer for evaluating magnetic anomalies due to finite three-dimensional bodies, *Geophys. Prospect.,* **11,** 292–299.

Carley, R.A., Whaler, K.A., Purucker, M.E. & Halekas, J.S., 2012. Magnetization of lunar crust, *J. geophys. Res.,* **117,** E08001, doi:10.1029/2011JE003944.

Dransfield, M.H., 1994. Airborne gravity gradiometry, *Ph.D thesis,* University of Western Australia.

Du, J.S., Chen, C., Liang, Q., Wang, H.R., Li, Y.G. & Lane, R., 2013. 3-D inversion of regional magnetic data in spherical coordinates and its preliminary application in Australia, *ASEG Extended Abstracts,* **1,** 1–4.

Du, J.S., Chen, C., Lesur, V., Li, Y.G., Lane, R., Liang, Q. & Wang, H.R., 2014. Three dimensional lithospheric magnetization structures beneath Australia derived by inverse modeling of CHAMP satellite magnetic field model, *Geophysical Research Abstracts,* Vol. 16, EGU2014-1315-1.

Dyment, J. & Arkani-Hamed, J., 1998a. Equivalent source magnetic dipoles revisited, *Geophys. Res. Lett.,* **25,** 2003–2006.

Dyment, J. & Arkani-Hamed, J., 1998b. Contribution of lithospheric remanent magnetization to satellite magnetic anomalies over the world's oceans, *J. geophys. Res.,* **103,** 15423–15441.

Finlay, C.C. *et al.*, 2010. International Geomagnetic Reference Field: the eleventh generation, *Geophys. J. Int.,* **183**(3), 1216–1230.

Fox Maule, C., Purucker, M., Olsen, N. & Mosegaard, K., 2005. Heat flux anomalies in Antarctica revealed by satellite magnetic data, *Science,* **309,** 464–467.

Grombein, T., Seitz, K. & Heck, B., 2010. *Untersuchung zur effizienten Berechnung topographisc-her Effekte auf den Gradiententensor am Fallbeispiel der Satellitengradiometriemission GOCE,* Rep 7547, KIT Scientific Reports, KIT Scientific Publishing, Karlsruhe, Germany, doi:10.5445/-KSP/1000017531.

Grombein, T., Seitz, K. & Heck, B., 2013. Optimized formulas for the gravitational field of a tesseroid, *J. Geodesy,* **87**(7), 645–660.

Grüninger, W., 1990. Zur topographisch-isostatischen Reduktion der Schwere, *Ph.D thesis,* Universität Karlsruhe.

Gubbins, D., Ivers, D., Masterton, S.M. & Winch, D.E., 2011. Analysis of lithospheric magnetization in vector spherical harmonics, *Geophys. J. Int.,* **187,** 99–117.

Hall, D.H., 1959. Direction of polarization determined from magnetic anomalies, *J. geophys. Res.,* **64**(11), 1945–1959.

Hansen, R.O. & Wang, X., 1988. Simplified frequency-domian expressions for potential fields of arbitrary three-dimensional bodies, *Geophysics,* **53,** 365–374.

Heck, B. & Seitz, K., 2007. A comparison of the tesseroid, prism and point-mass approaches for mass reductions in gravity field modeling, *J. Geodesy,* **81,** 121–136.

Heiskanen, W.A. & Moritz, H., 1967. *Physical Geodesy,* Freeman & Co.

Hemant, K. & Maus, S., 2005. Geological modeling of the new CHAMP magnetic anomaly maps using a Geophysical Information System (GIS) technique, *J. geophys. Res.,* **110,** B12, doi:10.10-29/2005JB003837.

Henderson, R.G. & Zietz, I., 1948. Analysis of total magnetic intensity anomalies produced by point and line sources, *Geophysics,* **13,** 428–436.

Jackson, A., 1990. Accounting for crustal magnetization in models of the core magnetic field, *Geophys. J. Int.,* **103,** 657–673.

Kim, J.W., Kim, H.R., von Frese, R., Taylor, P. & Rangelova, E., 2013. Geopotential field anomaly continuation with multi-altitude observations, *Tectonophysics,* **585,** 34–47.

Ku, C.C., 1977. A direct computation of gravity and magnetic anomalies caused by 2- and 3-dimensional bodies of arbitrary shape and arbitrary magnetic polarization by equivalent point method and a simplified cubic spline, *Geophysics,* **42,** 610–622.

Lane, R., 2009. Some issues and insights for gravity and magnetic modeling at the region to continent scale, *ASEG Extended Abstracts,* **1,** 1–11.

Langel, R.A. & Hinze, W.J., 1998. *The Magnetic Field of the Earth's Lithosphere: The Satellite Perspective,* Cambridge Univ. Press.

Li, Z.W., Hao, T.Y., Xu, Y. & Xu, Y., 2011. An efficient and adaptive approach for modeling gravity effects in spherical coordinates, *J. Appl. Geophys.,* **73,** 221–231.

Martinec, Z., 1998. *Boundary-Value Problems for Gravimetric Determination of a Precise Geoid*, *Lecture Notes in Earth Sciences,* **Vol. 73,** Springer-Verlag.

Masterton, S.M., Gubbins, D., Müller, R.D. & Singh, K.H., 2013. Forward modeling of oceanic lithospheric magnetization, *Geophys. J. Int.,* **192,** 951–962.

Meyer, J., Hufen, J.-H. & Siebert, M., 1985. On the identification of Magsat anomaly charts as crustal part of the internal field, *J. geophys. Res.,* **90,** 2537–2542.

Nolte, H.J. & Siebert, M., 1987. An analytical approach to the magnetic field of the Earth's crust, *J. Geophys.,* **61,** 69–76.

Parker, R.L., 1972. The rapid calculation of potential anomalies, *Geophys. J. R. astr. Soc.,* **31,** 447–455.

Parker, R.L., Shure, L. & Hildebrand, J.A., 1987. The application of inverse theory to seamount magnetism, *Rev. Geophys.,* **25,** 17–40.

Pedersen, L.B., 1985. The gravity and magnetic fields from ellipsoidal bodies in the wavenumber domain, *Geophys. Prospect.,* **33,** 263–281.

Purucker, M., Langel, R., Rajaram, M. & Raymond, C., 1998. Global magnetization models with a priori information, *J. Geophys. Res.,* **103**(B2), 2563–2584.

Purucker, M., Ravat, D., Frey, H., Voorhies, C., Sabaka, T. & Acuña, M., 2000. An altitude-normal -ized magnetic map of Mars and its interpretation, *Geophys. Res. Lett.,* **27**(16), 2449–2452.

Purucker, M., Langlais, B., Olsen, N., Hulot, G. & Mandea, M., 2002. The southern edge of cratonic North America: Evidence from new satellite magnetometer observations, *Geophys. Res. Lett.,* **29**(15), doi: 10.1029/2001GL013645.

Rao, D.B. & Babu, N.R., 1991. A rapid method for three-dimensional modeling of magnetic anomalies, *Geophysics,* **56**(11), 1729–1737.

Sharma, P.V., 1986. *Geophysical Methods in Geology,* Elsevier.

Singh, S.K. & Sabina, F.J., 1978. Magnetic anomaly due to a vertical right cylinder with arbitrary polarization, *Geophysics,* **43,** 173–178.

Stroud, A.H. & Secrest, D., 1966. *Gaussian Quadrature Formulas,* Prentice-Hall.

Talwani, M., 1965. Computation with help of a digital computer of magnetic anomalies caused by bodies of arbitrary shape, *Geophysics,* **30,** 797–817.

Tontini, F.C., Cocchi, L. & Carmisciano, C., 2009. Rapid 3-D forward model of potential fields with application to the Palinuro Seamount magnetic anomaly (southern Tyrrhenian Sea, Italy), *J. geophys. Res.,* **114,** B02103, doi:10.1029/2008JB005907.

Uieda, L., 2012. *Tesseroid Documentation,* Release 1.1-beta, Available at: http://tesseroids.leouieda.com, last accessed 30 March 2015.

Uieda, L., Bomfim, E.P., Braitenberg, C. & Molina, E., 2011. Optimal forward calculation method of the Marussi tensor due to a geologic structure at GOCE height, in *Proceedings of '4th International GOCE User Workshop',* Munich, Germany, 31 March-1 April 2011 (ESA SP-696, July 2011).

Vervelidou, F. & Thébault, E., 2014. A global estimate of the Earth's magnetic crustal thickness, *Geophysical Research Abstracts,* EGU General Assembly 2014, Vol. 16, EGU2014-6681-1.

von Frese, R.R.B., 1998. Correction to: R.R.B. von Frese, W.J. Hinze, L.W. Braile, 'Spherical Earth gravity and magnetic anomaly analysis by equivalent point source inversion, Earth and Planetary Science Letters 53 (1981) 69–83', *Earth planet. Sci. Lett.,* **163,** 409–411.

von Frese, R.R.B., Hinze, W.J. & Braile, L.W., 1981b. Spherical Earth gravity and magnetic anomaly analysis by equivalent point source inversion, *Earth planet. Sci. Lett.,* **53,** 69–83.

von Frese, R.R.B., Hinze, W.J., Braile, L.W. & Luca, A.J., 1981b. Spherical Earth gravity and magnetic anomaly modeling by Gauss-Legendre quadrature integration, *J. geophys. Res.,* **49,** 234–242.

von Frese, R.R.B., Hinze, W.J. & Braile, L.W., 1982. Regional North American gravity and magnetic anomaly correlations, *Geophys. J. R. astr. Soc.,* **69,** 745–761.

Wessel, P. & Smith, W.H.F., 1991. Free software helps map and display data, *EOS Trans. Am. geophys. Un.,* **72,** 441.

Whaler, K.A., 1994. Downward continuation of Magsat lithospheric anomalies to the Earth's surface, *Geophys. J. Int.,* **116,** 267–278.

Whaler, K.A. & Langel, R.A., 1996. Minimal crustal magnetizations from satellite data, *Phys. Earth planet. Inter.,* **98,** 303–319.

Whaler, K.A. & Purucker, M.E., 2005. A spatially continuous magnetization model for Mars, *J. geophys. Res.,* **110,** E09001, doi:10.1029/2004JE002393.

Wild-Pfeiffer, F., 2008. A comparison of different mass elements for use in gravity gradiometry, *J. Geod.,* **82,** 637–653.

Wild-Pfeiffer, F. & Heck, B., 2007. Comparison of the modelling of topographic and isostatic masses in the space and the frequency domain for use in satellite gravity gradiometry, in *Proceedings of the 1st Int. Symposium IGFS: Gravity Field of the Earth,* pp. 312–317, eds in Kilicoğlu, A. & Forsberg, R., Istanbul, Turkey, 2006, Harita Dergisi, Special Issue 18.

APPENDIX A: EXPRESSIONS FOR TAYLOR'S SERIES EXPANSION

The detailed expressions in eq. (21) are presented as follows:

$$K_u = \frac{\tau}{l^3}, \tag{A1}$$

$$K_v = x_i, \tag{A2}$$

$$L_v = \frac{3x_i x_j}{l^2} - \delta_{ij}, \tag{A3}$$

$$N_v = \frac{3}{l^4}\left(5x_i x_j x_k + \delta_{ijk} l^2 - x_k \delta_{ij} l^2\right), \tag{A4}$$

$$\partial_{r'} K_u = \frac{\partial K_u}{\partial r'} = \frac{1}{l^5}\left[2r' \cos\varphi' l^2 - 3\tau\left(r' - r\cos\psi\right)\right], \tag{A5}$$

$$\partial_{\varphi'} K_u = \frac{\partial K_u}{\partial \varphi'} = \frac{1}{l^5}\left(-r'^2 l^2 \sin\varphi' + 3\tau r r' \cos^{(\varphi')}\psi\right), \tag{A6}$$

$$\partial_{\lambda'} K_u = \frac{\partial K_u}{\partial \lambda'} = \frac{3\tau r r' \cos^{(\lambda')}\psi}{l^5}, \tag{A7}$$

$$\partial^2_{r'} K_u = \frac{\partial^2 K_u}{\partial r'^2} = \frac{\cos\varphi'}{l^6}\left[2l^3 - 6r' l^{(r')} l^2 - 9r'^2 l + 15r'^3 l^{(r')} + 3rr'\cos\psi\left(2l - 5r' l^{(r')}\right)\right], \tag{A8}$$

$$\partial^2_{\varphi'} K_u = \frac{\partial^2 K_u}{\partial \varphi'^2} = \frac{r'^2}{l^6}\left[-\cos\varphi' l^3 + 3\sin\varphi' l^{(\varphi')} l^2 + 3rr'\left(-l\sin\varphi'\cos^{(\varphi')}\psi + l\cos\varphi'\cos^{(\varphi'^2)}\psi - 5\cos\varphi' l^{(\varphi')}\cos^{(\varphi')}\psi\right)\right], \tag{A9}$$

$$\partial^2_{\lambda'} K_u = \frac{\partial^2 K_u}{\partial \lambda'^2} = \frac{3\tau r r'}{l^6}\left(l\cos^{(\lambda'^2)}\psi - 5l^{(\lambda')}\cos^{(\lambda')}\psi\right), \tag{A10}$$

$$\partial_m K_v = (x_i)^{(m)}, \quad \partial^2_m K_v = (x_i)^{(m^2)}, \qquad m = r', \varphi', \lambda', \tag{A11}$$

$$\partial_m L_v = \frac{\partial L_v}{\partial m} = \frac{3}{l^3}\left[(x_i x_j)^{(m)} l - 2x_i x_j l^{(m)}\right], \qquad m = r', \varphi', \lambda', \tag{A12}$$

$$\partial^2_m L_v = \frac{\partial^2 L_v}{\partial m^2} = \frac{3}{l^4}\left[(x_i x_j)^{(m^2)} l^2 - 4(x_i x_j)^{(m)} l^{(m)} l - 2x_i x_j l^{(m^2)} l + 6x_i x_j \left(l^{(m)}\right)^2\right], \qquad m = r', \varphi', \lambda', \tag{A13}$$

$$\partial_m N_v = \frac{\partial N_v}{\partial m}$$
$$= \frac{3}{l^5}\left\{5(x_i x_j x_k)^{(m)} l - 20 x_i x_j x_k l^{(m)}, \qquad m = r', \varphi', \lambda', + \left[(\delta_{ijk})^{(m)} - \delta_{ij}(x_k)^{(m)}\right] l^3 + 2(x_k \delta_{ij} - \delta_{ijk}) l^{(m)} l^2, \right\} \tag{A14}$$

$$\partial_m^2 N_v = \frac{\partial^2 N_v}{\partial m^2}$$
$$= \frac{3}{l^6}\left[5\left(x_i x_j x_k\right)^{(m^2)} l^2 - 40\left(x_i x_j x_k\right)^{(m)} l^{(m)} l\right.$$
$$- 20 x_i x_j x_k l^{(m^2)} l + 100 x_i x_j x_k \left(l^{(m)}\right)^2 \qquad , \qquad m = r', \varphi', \lambda', \tag{A15}$$
$$- \delta_{ij}\left(x_k\right)^{(m^2)} l^4 + 4\delta_{ij}\left(x_k\right)^{(m)} l^{(m)} l^3 + 2\delta_{ij} x_k l^{(m^2)} l^3 - 6 x_k \delta_{ij}\left(l^{(m)}\right)^2 l^2$$
$$\left. - 2\delta_{ijk} l^{(m^2)} l^3 + 6\delta_{ijk}\left(l^{(m)}\right)^2 l^2 - 4\left(\delta_{ijk}\right)^{(m)} l^{(m)} l^3 + \left(\delta_{ijk}\right)^{(m^2)} l^4\right]$$

$$l^{(r')} = \frac{\partial l}{\partial r'} = \frac{r' - r\cos\psi}{l}, \tag{A16}$$

$$l^{(\varphi')} = \frac{\partial l}{\partial \varphi'} = \frac{-r r' \cos^{(\varphi')}\psi}{l}, \tag{A17}$$

$$l^{(\lambda')} = \frac{\partial l}{\partial \lambda'} = \frac{-r r' \cos^{(\lambda')}\psi}{l}, \tag{A18}$$

$$l^{(r'^2)} = \frac{\partial^2 l}{\partial r'^2} = \frac{1}{l}\left[1 - \left(l^{(r')}\right)^2\right], \tag{A19}$$

$$l^{(\varphi'^2)} = \frac{\partial^2 l}{\partial \varphi'^2} = \frac{r r'}{l^2}\left(-l\cos^{(\varphi'^2)}\psi + l^{(\varphi')}\cos^{(\varphi')}\psi\right), \tag{A20}$$

$$l^{(\lambda'^2)} = \frac{\partial^2 l}{\partial \lambda'^2} = \frac{r r'}{l^2}\left(-l\cos^{(\lambda'^2)}\psi + l^{(\lambda')}\cos^{(\lambda')}\psi\right), \tag{A21}$$

$$\left(x_i x_j\right)^{(m)} = \frac{\partial}{\partial m}\left(x_i x_j\right) = \left(x_i\right)^{(m)} x_j + x_i\left(x_j\right)^{(m)}, \qquad m = r', \varphi', \lambda', \tag{A22}$$

$$\left(x_i x_j\right)^{(m^2)} = \frac{\partial^2}{\partial m^2}\left(x_i x_j\right) = \left(x_i\right)^{(m^2)} x_j + 2\left(x_i\right)^{(m)}\left(x_j\right)^{(m)} + x_i\left(x_j\right)^{(m^2)}, \qquad m = r', \varphi', \lambda', \tag{A23}$$

$$\left(x_i x_j x_k\right)^{(m)} = \frac{\partial}{\partial m}\left(x_i x_j x_k\right) = \left(x_i\right)^{(m)} x_j x_k + x_i\left(x_j\right)^{(m)} x_k + x_i x_j\left(x_k\right)^{(m)}, \qquad m = r', \varphi', \lambda', \tag{A24}$$

$$\left(x_i x_j x_k\right)^{(m^2)} = \frac{\partial^2}{\partial m^2}\left(x_i x_j x_k\right)$$
$$= \left(x_i\right)^{(m^2)} x_j x_k + 2\left(x_i\right)^{(m)}\left(x_j\right)^{(m)} x_k$$
$$+ 2\left(x_i\right)^{(m)} x_j\left(x_k\right)^{(m)} + x_i\left(x_j\right)^{(m^2)} x_k \qquad , \qquad m = r', \varphi', \lambda', \tag{A25}$$
$$+ 2 x_i\left(x_j\right)^{(m)}\left(x_k\right)^{(m)} + x_i x_j\left(x_k\right)^{(m^2)}$$

$$\left(\delta_{ijk}\right)^{(m)} = \begin{cases} -\left(x_i\right)^{(m)}, & i \neq j, j = k \\ -\left(x_j\right)^{(m)}, & j \neq i, i = k \\ -2\left(x_i\right)^{(m)}, & i = j, j = k \\ 0, \text{else} \end{cases}, \qquad m = r', \varphi', \lambda', \tag{A26}$$

$$\left(\delta_{ijk}\right)^{(m^2)} = \begin{cases} -\left(x_i\right)^{(m^2)}, & i \neq j, j = k \\ -\left(x_j\right)^{(m^2)}, & j \neq i, i = k \\ -2\left(x_i\right)^{(m^2)}, & i = j, j = k \\ 0, \text{ else} \end{cases}, \qquad m = r', \varphi', \lambda', \tag{A27}$$

$$\left(x_n\right)^{(m)} = \frac{\partial}{\partial m} x_n, \quad \left(x_n\right)^{(m^2)} = \frac{\partial^2}{\partial m^2} x_n, \quad m = r', \varphi', \lambda', n = i, j, k, \tag{A28}$$

$$\cos^{(\varphi')} \psi = \frac{\partial}{\partial \varphi'} \cos\psi = \sin\varphi \cos\varphi' - \cos\varphi \sin\varphi' \cos\left(\lambda' - \lambda\right), \tag{A29}$$

$$\cos^{(\varphi'^2)} \psi = \frac{\partial^2}{\partial \varphi'^2} \cos\psi = -\sin\varphi \sin\varphi' - \cos\varphi \cos\varphi' \cos\left(\lambda' - \lambda\right), \tag{A30}$$

$$\cos^{(\lambda')} \psi = \frac{\partial}{\partial \lambda'} \cos\psi = -\cos\varphi \cos\varphi' \sin\left(\lambda' - \lambda\right), \tag{A31}$$

$$\cos^{(\lambda'^2)} \psi = \frac{\partial^2}{\partial \lambda'^2} \cos\psi = -\cos\varphi \cos\varphi' \cos\left(\lambda' - \lambda\right), \tag{A32}$$

$$\frac{\partial}{\partial r'} x_1 = \cos\varphi \sin\varphi' - \sin\varphi \cos\varphi' \cos\left(\lambda' - \lambda\right), \tag{A33}$$

$$\frac{\partial}{\partial r'} x_2 = \cos\varphi' \sin\left(\lambda' - \lambda\right), \tag{A34}$$

$$\frac{\partial}{\partial r'} x_3 = -\cos\psi, \tag{A35}$$

$$\frac{\partial^2}{\partial r'^2} x_1 = \frac{\partial^2}{\partial r'^2} x_2 = \frac{\partial^2}{\partial r'^2} x_3 = 0, \tag{A36}$$

$$\frac{\partial}{\partial \varphi'} x_1 = r' \left[\cos\varphi \cos\varphi' + \sin\varphi \sin\varphi' \cos\left(\lambda' - \lambda\right)\right], \tag{A37}$$

$$\frac{\partial}{\partial \varphi'} x_2 = -r' \sin\varphi' \sin\left(\lambda' - \lambda\right), \tag{A38}$$

$$\frac{\partial}{\partial \varphi'} x_3 = -r' \cos^{\varphi'} \psi, \tag{A39}$$

$$\frac{\partial^2}{\partial \varphi'^2} x_1 = r' \left[-\cos\varphi \sin\varphi' + \sin\varphi \cos\varphi' \cos\left(\lambda' - \lambda\right)\right], \tag{A40}$$

$$\frac{\partial^2}{\partial \varphi'^2} x_2 = -r' \cos\varphi' \sin\left(\lambda' - \lambda\right), \tag{A41}$$

$$\frac{\partial^2}{\partial \varphi'^2} x_3 = -r' \cos^{(\varphi'^2)} \psi, \tag{A42}$$

$$\frac{\partial}{\partial \lambda'} x_1 = r' \sin\varphi \cos\varphi' \sin\left(\lambda' - \lambda\right), \tag{A43}$$

$$\frac{\partial}{\partial \lambda'} x_2 = r' \cos\varphi' \cos\left(\lambda' - \lambda\right), \tag{A44}$$

$$\frac{\partial}{\partial \lambda'} x_3 = -r' \cos^{(\lambda')} \psi, \tag{A45}$$

$$\frac{\partial^2}{\partial \lambda'^2} x_1 = r' \sin\varphi \cos\varphi' \cos\left(\lambda' - \lambda\right), \tag{A46}$$

$$\frac{\partial^2}{\partial \lambda'^2} x_2 = -r' \cos\varphi' \sin\left(\lambda' - \lambda\right), \tag{A47}$$

$$\frac{\partial^2}{\partial \lambda'^2} x_3 = -r' \cos^{(\lambda'^2)} \psi. \tag{A48}$$

APPENDIX B: EXPRESSIONS FOR RECTANGULAR PRISM

The detailed expressions in eqs (35)–(37) are presented as follows:

$$A_x = \eta' \ln\left(\zeta' + r\right) + \zeta' \ln\left(\eta' + r\right) - \xi' \arctan \frac{\eta'\zeta'}{\xi' r}, \tag{B1}$$

$$A_y = \zeta' \ln\left(\xi' + r\right) + \xi' \ln\left(\zeta' + r\right) - \eta' \arctan \frac{\xi'\zeta'}{\eta' r}, \tag{B2}$$

$$A_z = \xi' \ln\left(\eta' + r\right) + \eta' \ln\left(\xi' + r\right) - \zeta' \arctan \frac{\xi'\eta'}{\zeta' r}, \tag{B3}$$

$$A_{xx} = \arctan \frac{\left(\xi' - x_Q\right)\left(\eta' - y_Q\right)}{\left(\xi' - x_Q\right)^2 + r\left(\zeta' - z_Q\right) + \left(\zeta' - z_Q\right)^2}, \tag{B4}$$

$$A_{xy} = \ln\left[r + \left(\zeta' - z_Q\right)\right], \tag{B5}$$

$$A_{xz} = \ln\left[r + \left(\eta' - y_Q\right)\right], \tag{B6}$$

$$A_{yx} = A_{xy}, \tag{B7}$$

$$A_{yy} = -\arctan \frac{\left(\xi' - x_Q\right)\left(\eta' - y_Q\right)}{\left(\eta' - y_Q\right)^2 + r\left(\zeta' - z_Q\right) + \left(\zeta' - z_Q\right)^2}, \tag{B8}$$

$$A_{yz} = \ln\left[r + \left(\xi' - x_Q\right)\right], \tag{B9}$$

$$A_{zx} = A_{xz}, \tag{B10}$$

$$A_{zy} = A_{yz}, \tag{B11}$$

$$A_{zz} = -\arctan \frac{\left(\xi' - x_Q\right)\left(\eta - y_Q\right)}{r\left(\zeta' - z_Q\right)}, \tag{B12}$$

$$A_{xxx} = \frac{\partial A_{xx}}{\partial x_Q} = \frac{\left(\eta' - y_Q\right)\left[\left(\xi' - x_Q\right)^2 - r\left(\zeta' - z_Q\right)\right]}{r\left[\left(\xi' - x_Q\right)^2 + \left(\zeta' - z_Q\right)^2\right]\left[r + \left(\zeta' - z_Q\right)\right]}, \tag{B13}$$

$$A_{xxy} = \frac{\partial A_{xx}}{\partial y_Q} = \frac{-\left(\xi' - x_Q\right)}{r\left[r + \left(\zeta' - z_Q\right)\right]}, \tag{B14}$$

$$A_{xxz} = \frac{\partial A_{xz}}{\partial z_Q} = \frac{\left(\xi' - x_Q\right)\left(\eta' - y_Q\right)}{r\left[\left(\xi' - x_Q\right)^2 + \left(\zeta' - z_Q\right)^2\right]}, \tag{B15}$$

$$A_{xyx} = \frac{\partial A_{xy}}{\partial x_Q} = \frac{-\left(\xi' - x_Q\right)}{r\left[r + \left(\zeta' - z_Q\right)\right]}, \tag{B16}$$

$$A_{xyy} = \frac{\partial A_{xy}}{\partial y_Q} = \frac{-\left(\eta' - y_Q\right)}{r\left[r + \left(\zeta' - z_Q\right)\right]}, \tag{B17}$$

$$A_{xyz} = \frac{\partial A_{xy}}{\partial z_Q} = -\frac{1}{r}, \tag{B18}$$

$$A_{xzx} = \frac{\partial A_{xz}}{\partial x_Q} = \frac{-\left(\xi' - x_Q\right)}{r\left[r + \left(\eta' - y_Q\right)\right]}, \tag{B19}$$

$$A_{xzy} = \frac{\partial A_{xz}}{\partial y_Q} = -\frac{1}{r}, \tag{B20}$$

$$A_{xzz} = \frac{\partial A_{xz}}{\partial z_Q} = \frac{-\left(\zeta' - z_Q\right)}{r\left[r + \left(\eta' - y_Q\right)\right]}, \tag{B21}$$

$$A_{yyx} = \frac{\partial A_{yy}}{\partial x_Q} = \frac{-\left(\eta' - y_Q\right)}{r\left[r + \left(\zeta' - z_Q\right)\right]}, \tag{B22}$$

$$A_{yyy} = \frac{\partial A_{yy}}{\partial y_Q} = \frac{\left(\xi' - x_Q\right)\left[\left(\eta' - y_Q\right)^2 - r\left(\zeta' - z_Q\right)\right]}{r\left[\left(\eta' - y_Q\right)^2 + \left(\zeta' - z_Q\right)^2\right]\left[r + \left(\zeta' - z_Q\right)\right]}, \tag{B23}$$

$$A_{yyz} = \frac{\partial A_{yy}}{\partial z_Q} = \frac{\left(\xi' - x_Q\right)\left(\eta' - y_Q\right)}{r\left[\left(\eta' - y_Q\right)^2 + \left(\zeta' - z_Q\right)^2\right]}, \tag{B24}$$

$$A_{yzx} = \frac{\partial A_{yz}}{\partial x_Q} = -\frac{1}{r}, \tag{B25}$$

$$A_{yzy} = \frac{\partial A_{yz}}{\partial y_Q} = \frac{-\left(\eta' - y_Q\right)}{r\left[r + \left(\xi' - x_Q\right)\right]}, \tag{B26}$$

$$A_{yzz} = \frac{\partial A_{yz}}{\partial z_Q} = \frac{-\left(\zeta' - z_Q\right)}{r\left[r + \left(\xi' - x_Q\right)\right]}, \tag{B27}$$

$$A_{zzx} = \frac{\partial A_{zz}}{\partial x_Q} = \frac{-\left(\eta' - y_Q\right)\left(\zeta' - z_Q\right)}{r\left[\left(\xi' - x_Q\right)^2 + \left(\zeta' - z_Q\right)^2\right]}, \tag{B28}$$

$$A_{zzy} = \frac{\partial A_{zz}}{\partial y_Q} = \frac{-\left(\xi' - x_Q\right)\left(\zeta' - z_Q\right)}{r\left[\left(\eta' - y_Q\right)^2 + \left(\zeta' - z_Q\right)^2\right]}, \tag{B29}$$

$$A_{zzz} = \frac{\partial A_{zz}}{\partial z_Q} = -\frac{\left(\xi' - x_Q\right)\left(\eta' - y_Q\right)\left[r^2 + \left(\zeta' - z_Q\right)^2\right]}{r\left[\left(\xi' - x_Q\right)^2 + \left(\zeta' - z_Q\right)^2\right]\left[\left(\eta' - y_Q\right)^2 + \left(\zeta' - z_Q\right)^2\right]}. \tag{B30}$$